Second-order near trapping of water waves by a square array of vertical columns in bi-chromatic seas

Cong, Peiwen
State Key Laboratory of Coastal and Offshore Engineering, Dalian University of Technology

Zhao, Mingqiang
State Key Laboratory of Coastal and Offshore Engineering, Dalian University of Technology

Teng, Bin
State Key Laboratory of Coastal and Offshore Engineering, Dalian University of Technology

Gou, Ying
State Key Laboratory of Coastal and Offshore Engineering, Dalian University of Technology

他

出版情報：Journal of Fluids and Structures. 121, pp.103916-, 2023-08. Elsevier
バージョン：

Second-order near trapping of water waves by a square array of vertical columns in bi-chromatic seas

Peiwen Cong[a], Mingqiang Zhao[a], Bin Teng[a], Ying Gou[a], Yingyi Liu[b]

[a] State Key Laboratory of Coastal and Offshore Engineering, Dalian University of Technology, Dalian 116024, China

[b] Research Institute for Applied Mechanics, Kyushu University, Fukuoka 8168580, Japan

Abstract

Near trapping of water waves by an array of closely spaced columns is a hydrodynamic phenomenon with practical applications. A numerical investigation is conducted for the second-order interaction of bi-chromatic waves with a square array of vertical columns. The cross-sectional shape of the columns can be either circular or square with rounded corners. Numerical results indicate that a four-column cluster can amplify free-surface elevation through a near-trapping mechanism. Three lower-order near-trapped modes, namely p = 0, 2 and 3 modes, are primarily concerned, among which the amplification corresponding to the p = 2 mode is most pronounced. In addition, the four-column cluster can create both the linear and second-order near trappings. The latter could occur when the frequency sum of a pair of incident waves is consistent with the near-trapping frequency. The linear and second-order near-trapped modes own common characteristics. The second-order near-trapping response is predominated by the 'potential wave' component, while the 'quadratic wave' component plays a secondary role. Meanwhile, the effect of frequency difference on the mode shape in the second order is not evident. It is also noted that a decrease in the corner ratio can enhance the hydrodynamic interference effect among the columns and, in turn, evidently promote the near-trapping response for the p = 2 mode. An approximate approach is developed for the second-order near-trapping response, in which the 'quadratic wave' component is evaluated exactly. In contrast, the complicated 'potential wave' component corresponding to a pair of incident waves with distinct frequencies is approximated by that in monochromatic seas with the mean frequency. This approach is based on the hypothesis of weakly scattering of linear wave fields. Numerical results indicate that such approximation offers a reasonable alternative for the near-trapped modes in the low-frequency region.

Key Words:

Near trapping; bi-chromatic waves; second-order waves; square array

1. Introduction

Arrays of closely placed vertical columns have a wide range of applications in engineering practice. Examples include offshore platforms, bridges, floating airports and wave energy converter arrays. Previous studies have addressed the possibility that the waves diffracted by columns in close proximity could constructively interfere, causing apparently amplified free-surface oscillation between the columns in certain sea conditions (Evans and Porter, 1997; Malenica et al., 1999; Ohl et al., 2001a, 2001b). The large vertical water projection can cause severe structural damage, bringing about a long period of production downtime (Walker et al., 2008; Grice et al., 2013). Predicting the wave run-up and free-surface elevation is essential to determine an adequate airgap (height of the lower deck above mean sea level). Therefore, a deep understanding of the interaction of water waves with arrays of columns is of fundamental importance to ensure a successful design.

The pronounced wave-driven free-surface oscillation in the vicinity of the column array is a weakly damped hydrodynamic phenomenon, and the underlying physical mechanism has been studied extensively in the literature. Maniar and Newman (1997) studied wave diffraction by a long array of bottom-mounted circular columns. These columns are identical and equally spaced along the array. Numerical results revealed that the near-resonant free-surface motion could occur between the adjacent columns at critical wavenumbers, which is accompanied by the vastly amplified wave force on the columns. These near-trapped modes are associated with the existence of homogeneous solutions for an infinite column array, corresponding to trapped waves around a vertical column in a channel. For a finite array, homogeneous solutions no longer exist. Consequently, the free-surface oscillation around these critical wavenumbers becomes nearly resonant. This phenomenon is commonly referred to as near trapping. Evans and Porter (1997) concerned arrays of identical bottom-mounted circular columns with their axis at the corners of a regular polygon. Evans and Porter (1997) showed that the near-trapping phenomenon could also occur within the region internal to the polygon.

The near-trapping phenomenon has attracted considerable interest from many researchers. Early investigations are mainly based on analytical methods, such as the exact algebraic method by Kagemoto and Yue (1986) and the improved direct matrix method by Linton and Evans (1990). In addition, analytical methods have often been considered as the most suitable option to perform the optimization of wave energy parks with a large number of involved column-shaped devices (Göteman et al., 2015; Göteman, 2017). Analytical approaches take the obvious advantages of high efficiency, however, they have limitations in the treatment of structures with complex geometry. Therefore, numerical models have been developed for the analysis of near trapping for platforms incorporating large diameter columns, such as gravity-based multi-column platforms, and tension leg platforms (Walker et al., 2008; Cong et al., 2014; Grice et al., 2015; Ren et al., 2021; Zhang et al., 2022). Linearisation is the usual way to treat wave-body interaction, leading to a relatively more straightforward problem. Much work has looked at linear excitations, where the incoming wave frequency is around the near-trapping frequency. However, near trapping driven by nonlinear processes are also of practical interest. The strong hydrodynamic interference effect between the columns can reinforce the nonlinearity in the kinematic and dynamic free-surface boundary conditions, which results in an apparent nonlinear wave response. Malenica et al. (1999) developed a complete solution for second-order diffraction by an array of vertical circular columns in mono-chromatic seas. The empirical evidence of the results in Malenica et al. (1999) indicates that the near trapping in column arrays could also occur in second order when the frequency of the second-harmonic component of incident waves coincides with the near-trapping frequency. Such a phenomenon was referred to as second-order near trapping. Experimental confirmation of the presence of second-order near trapping for a four-column cluster or two rows of columns was provided by Ohl et al. (2001a, 2001b), Contento et al. (2005), Kagemoto et al. (2014), Cong et al. (2015). Experimental studies revealed the obvious effect of the second-order near trapping on the magnitude of local free surface oscillations as well as the scattered far-field radiation. Numerical investigations have also been conducted for the nonlinear near trapping based on the finite element method (Ma et al., 2001; Wang and Wu, 2007), boundary element method (Bai et al., 2014), and the cut-cell technique (Ning et al., 2022). Numerical results showed the amplified free-surface oscillation and wave force caused by the nonlinear near-trapping process. In addition to the open-sea cases, the linear wave trapping by an array of columns adjacent to an infinity long plane wall was investigated in Cong et al., (2020) by using the image theory, and then extended to the second-order near-trapping in Cong et al., (2021) by using the quadratic transfer functions (QTFs) in bi-directional waves. Numerical results showed that the reflected waves from the plane wall could cause the apparent reconstruction of the wave field around the columns, and lead to the noticeable near-trapped wave motion between the columns and the wall.

The near-trapping phenomenon is typically relevant to arrays of equally spaced columns. Rainbow trapping can be induced when the columns are with varying distances, i.e., a chirped column array. Rainbow trapping in a chirped column array has been investigated from theoretical studies (Peter et al., 2018, 2019) to model tests (Archer et al., 2019) and numerical modelling (Lu et al., 2021). It has been found that the frequencies of the wave group can be separated by a chirped column array and the wave energy is accumulated locally, whereas the evident wave amplification is of space-frequency dependence. Another interesting phenomenon associated with a column array is cloaking. A creative cloaking phenomenon has been found by Newman (2013, 2014) for the configuration of an interior circular column regularly surrounded by several exterior circular columns. This phenomenon is characterised by the absence of scattered waves radiating to infinity; the cloaked structure appears invisible to a far-field observer. The corresponding wave drift force acting on the entire structure becomes very small. The significant reduction of the wave drift force owing to cloaking has been experimentally confirmed by Kashiwagi et al. (2015) and Zhang et al. (2019). Meanwhile, optimisation of the geometric dimensions and the configuration of the outer columns have been conducted to achieve broadband cloaking (Zhang et al., 2020a) and the simultaneous realisation of the wave energy concentration (Zhang et al., 2020b).

The multi-column structures can be designed to tune the near-trapping frequencies above and/or below that at which significant ocean wave energy is present. This can avoid the significant free-surface responses at the wave frequencies due to linear excitations. However, previous results indicated that the second-order responses could contribute noticeably to the overall free-surface elevation. When the second-order effect is included in the presence of irregular waves, there are excitations at both the sum or difference frequencies for all possible pairs of incident wave frequency components. The sum- and difference-frequency excitations cover a broad frequency range, and they may be of primary concern when the near trapping is excited by them. The phenomenon of near trapping has been investigated in various works; however, the vast majority of these works are restricted to mono-chromatic waves. Grice et al. (2015) investigated the extreme free-surface elevations around the gravity-based multi-column platforms to second order using the QTFs in bi-chromatic seas. However, the characteristic of the second-order wave fields subject to bi-chromatic excitation has not been discussed. To the best of the authors' knowledge, no data have yet been published for the second-order near-trapped wave fields subject to bi-chromatic excitations. In light of the above, the main objective of this study is to promote a deep understanding of second-order near trapping in bi-chromatic waves.

A numerical model for the second-order bi-chromatic wave diffraction by arbitrarily-shaped three-dimensional bodies is developed based on a high-order boundary element method with successful treatment of singular and nearly singular integrals. In addition to the systematic convergence tests, numerical results are validated against semi-analytic solutions. Numerical and theoretical investigations are then conducted for the near trapping of water waves by a square array of vertical columns. Attention has been paid to the second-order near-trapped modes subject to bi-chromatic excitations. Three lower-order near-trapped modes, namely $p = 0$, 2 and 3 modes, are primarily concerned. In addition, a number of physical parameters critical to the free-surface oscillation are examined in detail, including the cross-sectional shape of the columns and the frequency combination of the incident waves. Their effects on the second-order near-trapped wave motion have been discussed. These investigations provide new insights into the near-trapping phenomenon of offshore multi-column structures.

The remaining part of this study is organised as follows. Following the introduction, Section 2 presents the expression of the second-order free-surface elevation in bi-chromatic seas. The numerical approach to the second-order free-surface elevation in bi-chromatic seas is described in Section 3. In Section 4, theoretical investigation of the trapped modes of a square array of circular columns is conducted. Then, the second-order near trapping subject to bi-chromatic excitations is investigated in Section 5. Finally, conclusions are drawn in Section 6.

2. Expression of the second-order free-surface elevation in bi-chromatic seas

The wave diffraction caused by an arbitrary, three-dimensional body in bi-chromatic seas is considered. A space-fixed coordinate system *oxyz* is used. *oxyz* has the *z*-axis pointing vertically upwards, and its original is at the undisturbed free surface. The usual framework of potential flow theory is adopted. Then, a velocity potential Φ can be used to describe the fluid velocity vector, and the velocity potential has to satisfy Laplace's equation

$$\nabla^2\Phi = \frac{\partial^2\Phi}{\partial x^2} + \frac{\partial^2\Phi}{\partial y^2} + \frac{\partial^2\Phi}{\partial z^2} = 0. \tag{1}$$

The velocity potential, satisfying a nonlinear boundary condition, can be expressed as a perturbation expression in terms of the wave steepness ε, truncated at the second order. That is

$$\Phi = \varepsilon\Phi^{(1)} + \varepsilon^2\Phi^{(2)} + O\left(\varepsilon^3\right). \tag{2}$$

Similarly, the free-surface elevation ζ can be expanded into the following form:

$$\zeta = \varepsilon\zeta^{(1)} + \varepsilon^2\zeta^{(2)} + O\left(\varepsilon^3\right). \tag{3}$$

In Eqs. (2) and (3), the subscripts (1) and (2) are used to denote the first- and second-order quantities with respect to the wave steepness ε, respectively.

When a body is placed in bi-chromatic incident waves with the frequencies ω_1 and ω_2, the total first-order velocity potential can be decomposed into the following form:

$$\Phi^{(1)}\left(\mathbf{x},\ t\right)=\mathrm{Re}\left\{\sum_{j=1}^{2}\left[\phi_j^{(1)}\left(\mathbf{x},\ \omega_j\right)\mathrm{e}^{-\mathrm{i}\omega_j t}\right]\right\}, \tag{4}$$

where $\phi_j^{(1)}$ is the first-order spatial potential at the frequency ω_j; $\mathbf{x} = (x, y, z)^T$ is the position vector of the field point. Meanwhile, the second-order velocity potential can be expressed as the superposition of the sum- and difference-frequency terms. That is

$$\Phi^{(2)}\left(\mathbf{x},\ t\right)=\mathrm{Re}\left\{\sum_{j=1}^{2}\sum_{l=1}^{2}\left[\phi_{jl}^{(2)+}\left(\mathbf{x},\ \omega_j+\omega_l\right)e^{-\mathrm{i}\left(\omega_j+\omega_l\right)t}+\phi_{jl}^{(2)-}\left(\mathbf{x},\ \omega_j-\omega_l\right)e^{-\mathrm{i}\left(\omega_j-\omega_l\right)t}\right]\right\}, \tag{5}$$

where $\phi_{jl}^{(2)+}$ and $\phi_{jl}^{(2)-}$ refer to the second-order spatial potentials at the frequencies of $\omega_j+\omega_l$ and $\omega_j-\omega_l$, respectively.

Similar to the velocity potential, the first- and second-order free-surface elevation can be expressed as

$$\zeta^{(1)}\left(x,\ y,\ t\right)=\mathrm{Re}\left[\sum_{j=1}^{2}\eta_j^{(1)}\left(x,\ y,\ \omega_j\right)\mathrm{e}^{-\mathrm{i}\omega_j t}\right], \tag{6}$$

and

$$\begin{aligned}\zeta^{(2)}\left(x,\ y,\ t\right)=\mathrm{Re}\left\{\sum_{j=1}^{2}\sum_{l=1}^{2}\left[\eta_{jl}^{(2)+}\left(x,\ y,\ \omega_j+\omega_l\right)e^{-\mathrm{i}\left(\omega_j+\omega_l\right)t}\right.\right.\\ \left.\left.+\eta_{jl}^{(2)-}\left(x,\ y,\ \omega_j-\omega_l\right)e^{-\mathrm{i}\left(\omega_j-\omega_l\right)t}\right]\right\},\end{aligned} \tag{7}$$

where $\eta_j^{(1)}$, $\eta_{jl}^{(2)+}$ and $\eta_{jl}^{(2)-}$ are the complex amplitudes of the free-surface elevation. On the free surface, both kinematic and dynamic boundary conditions exist. The former requires that no fluid can be transported across the free surface. While the latter requires that the pressure on the free surface is uniform and equal to the external atmospheric pressure, which is assumed to be zero. Then, on $z = \zeta$, we can have

$$\frac{\partial\zeta}{\partial t}+\frac{\partial\Phi}{\partial x}\frac{\partial\zeta}{\partial x}+\frac{\partial\Phi}{\partial y}\frac{\partial\zeta}{\partial y}=\frac{\partial\Phi}{\partial z}, \tag{8a}$$

and

$$\frac{\partial \Phi}{\partial t} + g\zeta + \frac{1}{2}\nabla\Phi \cdot \nabla\Phi = 0. \tag{8b}$$

When the amplitude of wave motion is small, the kinematic and dynamic boundary conditions can be satisfied on the undisturbed free surface (z = 0) by carrying out the Taylor series expansion. Then, after inserting Eqs. (6) and (7) into Eq. (8b) and collecting the terms in the same order of ε, we can have

$$\eta_j^{(1)} = \frac{\mathrm{i}\omega_j}{g}\phi_j^{(1)}\Big|_{z=0}. \quad (j = 1,\ 2) \tag{9}$$

In the meantime, the second-order free-surface elevation contains two distinct parts, which are contributed from the second-order velocity potential and driven by the interaction between linear components in local wave fields, respectively. Then, we can have:

$$\eta_{jl}^{(2)\pm} = \eta_{jl,\,p}^{(2)\pm} + \eta_{jl,\,q}^{(2)\pm}. \quad (j,\ l = 1,\ 2) \tag{10}$$

In Eq. (10), the subscripts 'p' and 'q' are used to denote these two parts. Hereinafter, these two parts are referred to as the 'potential wave' component and 'quadratic wave' component, respectively, and they are defined by

$$\eta_{jl,\,p}^{(2)\pm} = \frac{\mathrm{i}\left(\omega_j \pm \omega_l\right)}{g}\phi_{jl,\,p}^{(2)\pm}\Big|_{z=0}, \tag{11}$$

and

$$\eta_{jl,\,q}^{(2)+} = \frac{1}{4g}\left[-\frac{\omega_j\omega_l}{g}\left(\frac{\omega_j^2}{g} + \frac{\omega_l^2}{g}\right)\phi_j^{(1)}\phi_l^{(1)} - \nabla\phi_j^{(1)} \cdot \nabla\phi_l^{(1)}\right]\Bigg|_{z=0}; \tag{12a}$$

$$\eta_{jl,\,q}^{(2)-} = \frac{1}{4g}\left[\frac{\omega_j\omega_l}{g}\left(\frac{\omega_j^2}{g} + \frac{\omega_l^2}{g}\right)\phi_j^{(1)}\phi_l^{(1)*} - \nabla\phi_j^{(1)} \cdot \nabla\phi_l^{(1)*}\right]\Bigg|_{z=0}. \tag{12b}$$

Meanwhile, the following symmetric relation is held by the sum- and difference-frequency free-surface elevation amplitude:

$$\eta_{jl}^{(2)+} = \eta_{lj}^{(2)+}; \quad \eta_{jl}^{(2)-} = \eta_{lj}^{(2)-*}. \tag{13}$$

3. Numerical evaluation of the second-order free-surface elevation subject to bi-

chromatic incident waves

As shown in Eqs. (9)~(12), the free-surface elevation amplitude can be determined using the velocity potential on the free surface. For the wave interaction with stationary bodies, the velocity potential can be expressed in terms of the incident and diffraction potentials. That is

$$\phi_j^{(1)} = \phi_{j,\,I}^{(1)} + \phi_{j,\,D}^{(1)}, \quad (j=1,\ 2) \tag{14a}$$

$$\phi_{jl}^{(2)\pm} = \phi_{jl,\,I}^{(2)\pm} + \phi_{jl,\,D}^{(2)\pm}, \quad (j,\ l=1,\ 2) \tag{14b}$$

The detailed expressions of the first-order incident potential $\phi_{j,\,I}^{(1)}$ and the second-order sum- and difference-frequency incident potentials $\phi_{jl,\,I}^{(2)\pm}$ have been derived in previous studies, such as Kim and Yue (1990). If the classical Green second identity is applied and relevant boundary conditions are employed, we can have the following equations:

$$\phi_{j,\,D}^{(1)}(\mathbf{x}_0)\Big|_{z_0=0} = \iint_{S_b} \left[\frac{\partial G(\mathbf{x},\ \mathbf{x}_0,\ \omega_j)}{\partial n} \phi_{j,\,D}^{(1)}(\mathbf{x}) + G(\mathbf{x},\ \mathbf{x}_0,\ \omega_j) \frac{\partial \phi_{j,\,I}^{(1)}(\mathbf{x})}{\partial n} \right] \mathrm{d}s; \tag{15a}$$

$$\phi_{jl,\,D}^{(2)\pm}(\mathbf{x}_0)\Big|_{z_0=0} = \iint_{S_b} \left[\frac{\partial G(\mathbf{x},\ \mathbf{x}_0,\ \omega_j \pm \omega_l)}{\partial n} \phi_{jl,\,D}^{(2)\pm}(\mathbf{x}) + G(\mathbf{x},\ \mathbf{x}_0,\ \omega_j \pm \omega_l) \frac{\partial \phi_{jl,\,I}^{(2)\pm}(\mathbf{x})}{\partial n} \right] \mathrm{d}s + I_{jl,\,f}^{(2)\pm}(\mathbf{x}_0). \tag{15b}$$

where

$$I_{jl,\,f}^{(2)\pm}(\mathbf{x}_0) = -\frac{1}{g} \iint_{S_f} \left[G(\mathbf{x},\ \mathbf{x}_0,\ \omega_j \pm \omega_l) \cdot Q_{D,\,jl}^{(2)\pm}(\mathbf{x}) \right]\Big|_{z=0} \mathrm{d}s. \tag{16}$$

In Eqs. (14) and (15), $\mathbf{x}_0 = (x_0, y_0, z_0)^T$ is the position vector of the source point.

For the derivation of Eq. (15), the oscillating source G, which satisfies the linear free-surface condition, the Sommerfeld condition at infinity and the no-flow condition on the horizontal seabed, has been used as Green's function. The second-order diffraction potential $\phi_{jl,\,D}^{(2)\pm}$ represents the combined potential owing to the second-order incident waves as well as the free-surface forcing term $Q_{jl,\,D}^{(2)\pm}$. $Q_{jl,\,D}^{(2)\pm}$ is due to all the quadratic contributions of the first-order quantities on the free surface. $Q_{jl,\,D}^{(2)\pm}$ can be decomposed into the following symmetric form:

$$Q_{jl,D}^{(2)\pm} = \frac{1}{2}\left(Q_{jl}^{(2)\pm} + Q_{lj}^{(2)\pm}\right), \tag{17}$$

where

$$\begin{aligned} Q_{jl}^{(2)+} = & -\frac{\mathrm{i}\omega_l}{2g}\phi_l^{(1)}\left(-\omega_j^2\frac{\partial\phi_j^{(1)}}{\partial z} + g\frac{\partial^2\phi_j^{(1)}}{\partial z^2}\right) + \mathrm{i}\omega_l\nabla\phi_l^{(1)}\cdot\nabla\phi_j^{(1)} \\ & + \frac{\mathrm{i}\omega_l}{2g}\phi_{l,I}^{(1)}\left(-\omega_j^2\frac{\partial\phi_{j,I}^{(1)}}{\partial z} + g\frac{\partial^2\phi_{j,I}^{(1)}}{\partial z^2}\right) - \mathrm{i}\omega_l\nabla\phi_{l,I}^{(1)}\cdot\nabla\phi_{j,I}^{(1)}; \end{aligned} \tag{18a}$$

$$\begin{aligned} Q_{jl}^{(2)-} = & \frac{\mathrm{i}\omega_l}{2g}\phi_l^{(1)*}\left(-\omega_j^2\frac{\partial\phi_j^{(1)}}{\partial z} + g\frac{\partial^2\phi_j^{(1)}}{\partial z^2}\right) - \mathrm{i}\omega_l\nabla\phi_l^{(1)*}\cdot\nabla\phi_j^{(1)} \\ & - \frac{\mathrm{i}\omega_l}{2g}\phi_{l,I}^{(1)*}\left(-\omega_j^2\frac{\partial\phi_{j,I}^{(1)}}{\partial z} + g\frac{\partial^2\phi_{j,I}^{(1)}}{\partial z^2}\right) + \mathrm{i}\omega_l\nabla\phi_{l,I}^{(1)*}\cdot\nabla\phi_{j,I}^{(1)}. \end{aligned} \tag{18b}$$

The right-hand side of Eq. (15) involves the integration of the potential over the body surface. Details for the solution of the first- and second-order diffraction potentials over the body surface for mono-chromatic and bi-chromatic seas can be found in previous studies, such as Eatock Taylor and Chau (1992) and Teng and Cong (2017). Hence, they are not discussed here for brevity. Due to the interference effect, the nonlinearity is intuitively expected to be strong in the immediate vicinity of the columns. Refined meshes should be used to capture the rapid variation of the free-surface elevation. Then, under some conditions, $\mathbf{x}_0$ can be very close to the body surface S_b, leading to a nearly singular integration. The self-adaptive Gauss integration method (Sun et al., 2007) is adopted to overcome the difficulty associated with the nearly singular integration. It requires that when the nearly singular integration happens within a specific element, this element will be subdivided into a series of finer elements with a smaller size. The subdivision will not stop until the characteristic size of each sub-element is equal to or smaller than the distance between the source and field points.

Eq. (15) notes that the main difference between the first- and second-order solutions lies in the evaluation of $I_{jl,f}^{(2)\pm}$. The entire free surface is divided into three regions to evaluate this complex integral. The near-field water plane is bounded by the waterline and an exterior circular boundary. Within this region, the free surface is discretised into a series of quadratic surface elements, and the integration is performed numerically based on a quadrature formula. Within the middle-field region, Green's function is given in the form of a discrete eigenfunction expansion by using Graf's addition theorem. In addition, the velocity potential is expanded into a Fourier series with respect to the polar angle θ. The free surface integral is simplified into a series of radial integrals that can be integrated numerically. In the outermost region, the integral is transformed to another form in conjunction with some residuals. Using the asymptotic expansion of the Hankel function, the new integral is further reduced to one whose integrand is represented by the summation of polynomials of various orders, and each term of the polynomials can be integrated analytically.

The convergence of the results with respect to the mesh discretisation is examined to confirm the accuracy of the numerical model. Two test cases are primarily concerned. The first test case involves an array of four bottom-standing circular columns of radius a = 10 m in the water of depth $h = 3a$. The centres of the columns are located at ($\pm 2a$, $\pm 2a$) on the quiescent free surface. The configuration of this column array is given in Fig. 1(a). In the second one, an array of rounded-corner square columns is considered. The side length of the cross-section of the columns is $2a$ = 20 m, and the radius of the rounded corner is R. The configuration of such a column array is shown in Fig. 1(b). As shown in Fig. 1, the columns in the array are numbered clockwise, with column 1 located in the first quadrant. Local coordinate systems ($o_jx_jy_jz_j$) and ($o_jr_j\theta_jz_j$) (j = 1, 2, …, 4) have been defined at each column. In addition, in Fig. 1, β is the heading angle of incident waves with respect to positive the x-axis. Numerical computation is then conducted for the second-order sum- and difference-frequency wave run-up along the columns for different frequency pairs. Two geometric symmetry planes are adopted to facilitate the computation. In addition, two meshing schemes, namely 'Mesh 1' and 'Mesh 2', have been adopted for each test case. For 'Mesh 1', 480 elements on the body surface and 352 elements in the near-field water plane area with an exterior radius of 75 m. For 'Mesh 2', 960 elements on the body surface and 816 elements in the near-field water plane area with an exterior radius equal to 90 m. As an example, the mesh discretisations for an array of rounded-corner square columns are depicted in Fig. 2. Figs. 3~4 show the variation of the sum- and difference-frequency wave runup which occurs at the intersection of the column 1 and the free surface. As shown in Figs. 3~4, there is good agreement between the results based on different mesh discretisations, which suggests that convergence is achieved.

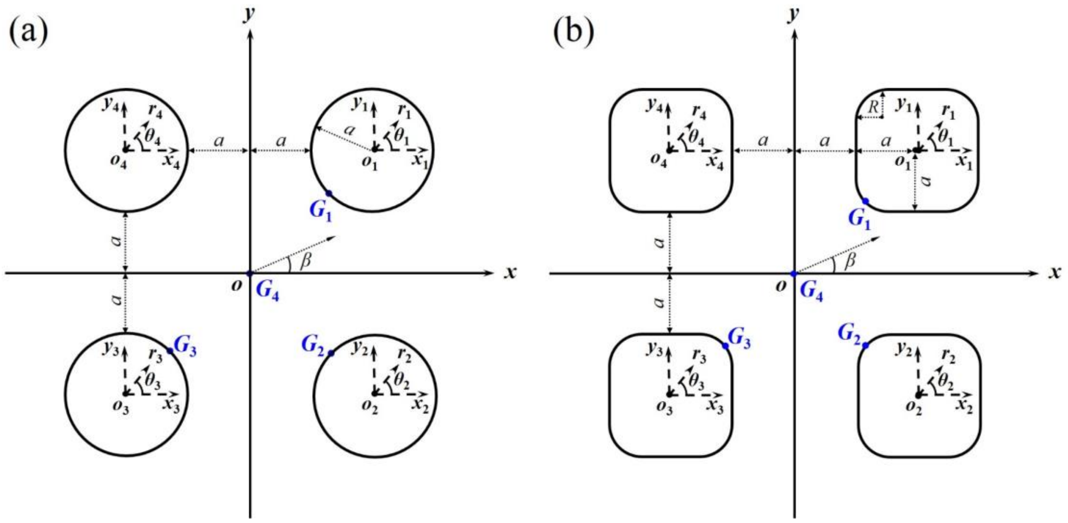

Fig. 1 Configuration of an array of (a) circular columns and (b) rounded-corner square columns

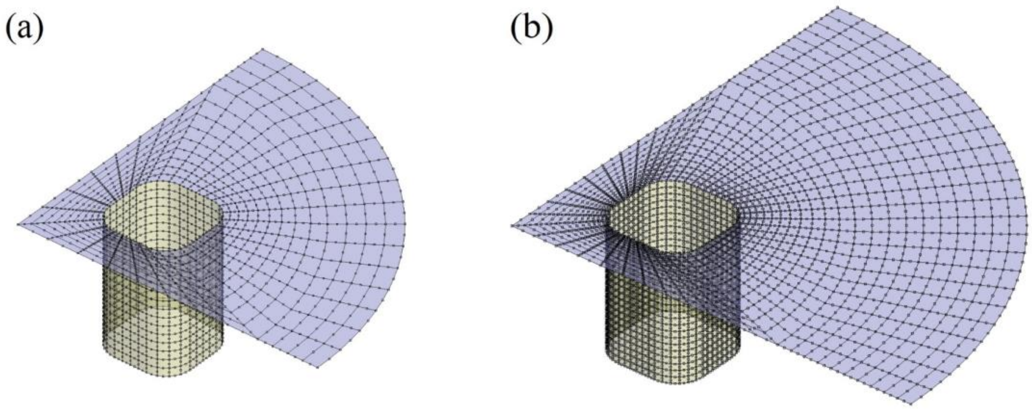

Fig. 2 Mesh discretisations for an array of rounded-corner square columns based on the meshing schemes: (a) 'Mesh 1' and (b) 'Mesh 2', respectively.

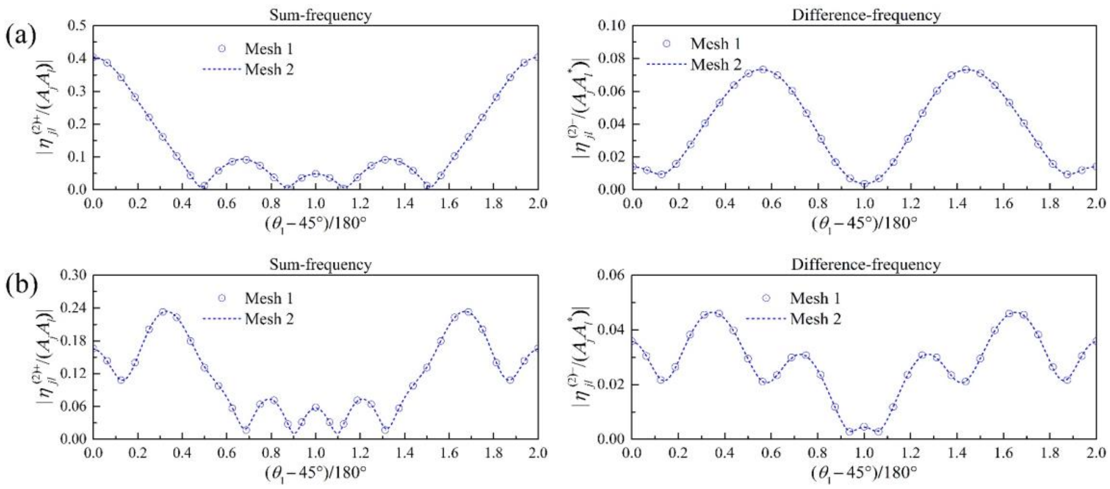

Fig. 3 Comparison of the sum- and difference-frequency wave run-up for an array of circular columns with β = 45° for (a) (ω_j, ω_l) = (0.6, 0.8), and (b) (ω_j, ω_l) = (0.8, 1.2).

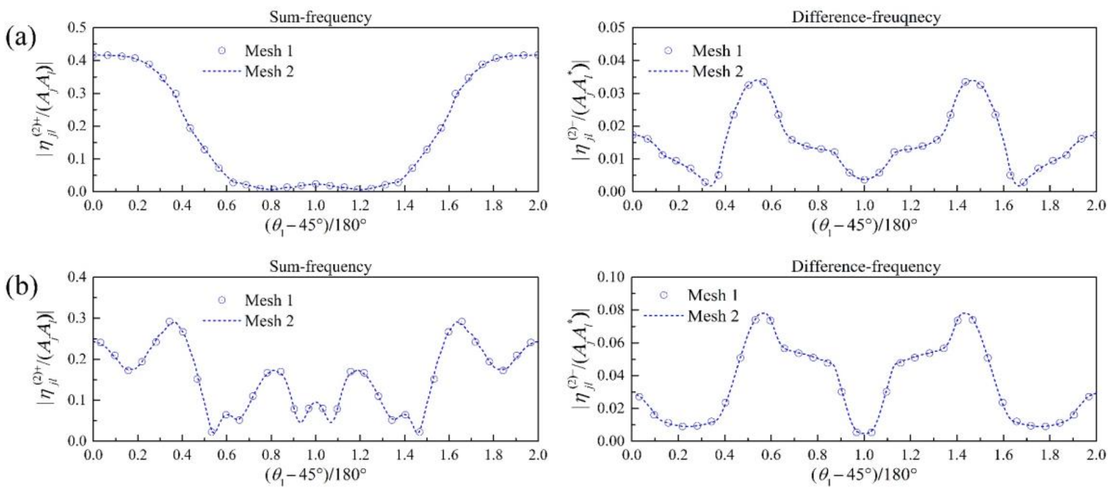

Fig. 4 Comparison of the (a) sum- and (b) difference-frequency wave run-up for an array of rounded-corner square columns (R = 6 m) with β = 45° for: (a) (ω_j, ω_l) = (0.6, 0.8), and (b) (ω_j, ω_l) = (0.8, 1.2).

To further verify the reliability of the present results, a comparison with the published data is conducted. A vertical circular column of radius a in the water of depth h = 4a is considered. Numerical computation is then performed for the frequency pair $\left(v_j a,\ v_l a\right)$ = (1.4, 1.6), where $v_{j(l)}a = \omega_{j(l)}^2 / g$. In addition, the incident waves travel along the positive x-axis. In the computation, 410 quadrilateral elements are used in each quadrant (210 elements on the body surface and 200 elements in the near-field water plane area with an exterior radius of 6a). The results of the second-order sum- and difference-frequency wave run-up along the column are shown in Fig. 5. The semi-analytical results based on a ring-source integral equation method (Kim and Yue, 1990) have also been shown for comparison. There is good agreement between the present results and the semi-analytical results, which further confirms the validity of the present model.

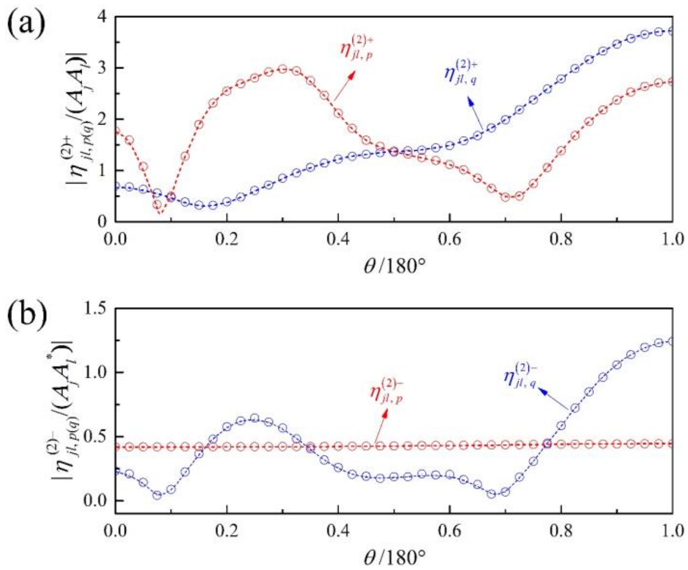

Fig. 5 Comparison of the second-order (a) sum- and (b) difference-frequency wave run-up components, i.e., the 'potential wave' component $\eta_{jl,p}^{(2)\pm}$ and the 'quadratic wave' component $\eta_{jl,q}^{(2)\pm}$, along a vertical column of radius a in the water of h = 4a for $\left(v_j a,\ v_l a\right)$ = (1.4, 1.6). The lines and symbols represent the present results and those in Kim and Yue (1989), respectively.

4. Trapped modes of a square array of circular columns

Before investigating near trapping, it is essential to find the wave frequencies most likely to respond violently by identifying the trapped-mode wavenumbers for specified structures. The trapped-mode wavenumbers are defined as those at which the pure wave trapping occurs (with no waves radiated away from the structure). Evans and Porter (1997) developed a theoretical method to predict the wavenumbers for pure wave trapping and the associated mode shapes based on the Fourier–Bessel expansion of the velocity potential. Meylan and Eatock Taylor (2009) investigated the trapped modes in the time domain for arbitrary initial displacements by using the generalised eigenfunction expansion. For more general configurations, such as semi-submersibles, an approximation method was developed by Grice et al. (2015) using the symmetric and antisymmetric properties of the mode shapes.

An array of four bottom-standing circular columns is then considered. Its configuration is given in Fig. 1(a), similar to that used in Malenica et al. (1999). The elegant method of Evans and Porter (1997) is suitable for this configuration, and hence it is used. The total wave field resulting from the wave-structure interaction is modelled by a Fourier–Bessel series. By allowing the frequency to be complex, it is possible to identify the wavenumber theoretically at which a phenomenon of pure wave trapping occurs. A violent response could happen when the matrix of coefficients associated with the expansion series has a determinant close to zero. The wavenumbers leading to a zero in the determinant are the trapped-mode wavenumbers. The trapped-mode wavenumbers are often complex. The value of the imaginary part gives a measure of the wave damping due to radiation to infinity. In a complex space with the imaginary part in [–0.2, 0], the first three trapped-mode wavenumbers have been found, which are ka = (0.484, –0.140), (1.671, –0.094) and (4.404, –0.145), respectively.

The mode shapes of the three trapped modes are shown in Figs. 6~8, respectively. Fig. 6 shows a mode shape which does not vary apparently along the circumferential direction within the region internal to the column array. The internal fluid oscillates almost uniformly and behaves like a rigid body. In contrast, Fig. 7 exhibits a mode shape characterised by a 2 × 2 arrangement of peaks and troughs formed in the area close to the column surfaces. Troughs are created around neighbouring columns simultaneously when an apparent peak appears in the vicinity of a certain column in the array. This in turn creates a $\begin{pmatrix} + & - \\ - & + \end{pmatrix}$ wave pattern. A more complicated mode shape is shown in Fig. 8. The remarkable peaks and troughs formed in the vicinity of the columns are in a $\begin{pmatrix} - & + \\ - & + \end{pmatrix}$ pattern. In addition, another 3 × 2 arrangement of peaks and troughs is included in the central region of the internal free surface. They are symmetric with respect to the x-axis while symmetric with respect to the y-axis, creating a $\begin{pmatrix} + & - \\ - & + \\ + & - \end{pmatrix}$ wave pattern.

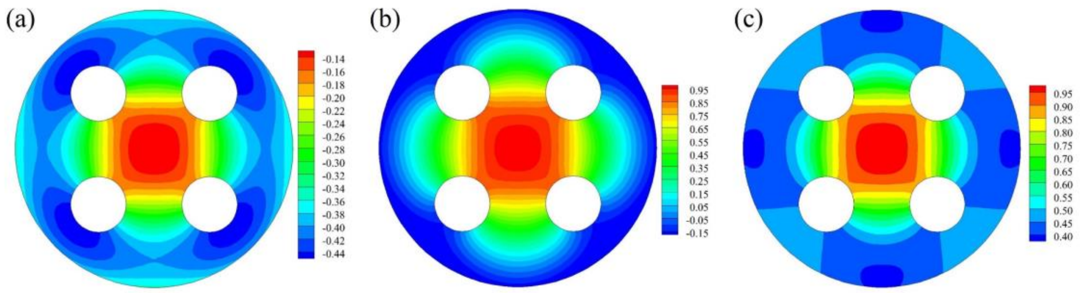

Fig. 6 Mode shape for an array of four bottom-standing circular columns with ka = (0.484, –0.140) and β = 45°: (a) real part, (b) imaginary part, and (c) modulus

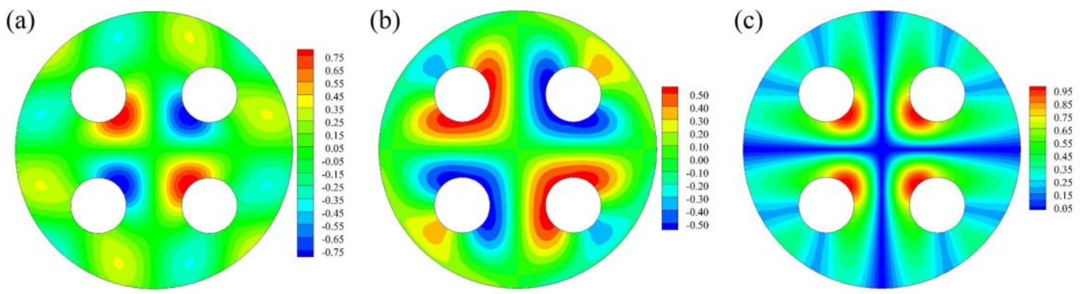

Fig. 7 Mode shape for an array of four bottom-standing circular columns with ka = (1.671, –0.094) and β = 45°: (a) real part, (b) imaginary part, and (c) modulus

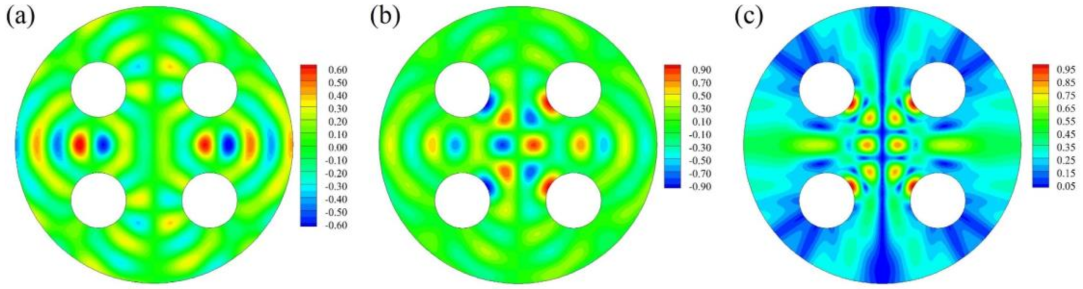

Fig. 8 Mode shape for an array of four bottom-standing circular columns with ka = (4.404, –0.145) and β = 0°: (a) real part, (b) imaginary part, and (c) modulus

5. Near trapping of water waves by a square array of vertical columns

Near trapping can be considered the situation if one sets the imaginary part of these complex wavenumbers to zero. Each near-trapping frequency is associated with a mode of strong local free-surface oscillation. It is close to the pure wave-trapping, but still with wave radiation leaking out to infinity. In this section, an investigation is conducted for the near trapping of water waves by a four-column structure. The cross-sectional shape of the columns can be either circular or square with round corners.

5.1 Linear near trapping and near-trapped modes

First, the linear near trapping by a square array of circular columns are concerned. The configuration is the same as that in Fig. 1(a). Linear near trapping is induced by the first-order mono-chromatic incident waves, which can be regarded as a limiting case of bi-chromatic waves with $\omega_j = \omega_l = \omega$ and $A_j = A_l = A$. In view of this, in this section, the subscripts 'j' and 'l' are removed from the symbols of the free-surface elevation and other physical quantity for simplicity. Fig. 9 depicts the variation of the first-order wave run-up amplitude along the downstream column (in Quadrant 1) for β = 45°. When β = 45°, the four columns form a diamond arrangement with respect to the direction of wave propagation. It clearly shows the occurrence of peak wave run-ups at ω = 0.652, 1.280 and 2.078 rad/s, respectively. The wavenumbers corresponding to the three wave frequencies are k = 0.0484, 0.1671 and 0.4404 m^{-1}, respectively, which are close to the real part of the complex trapped-mode wavenumbers. It indicates that the peak wave run-ups are induced by the near trapping of water waves.

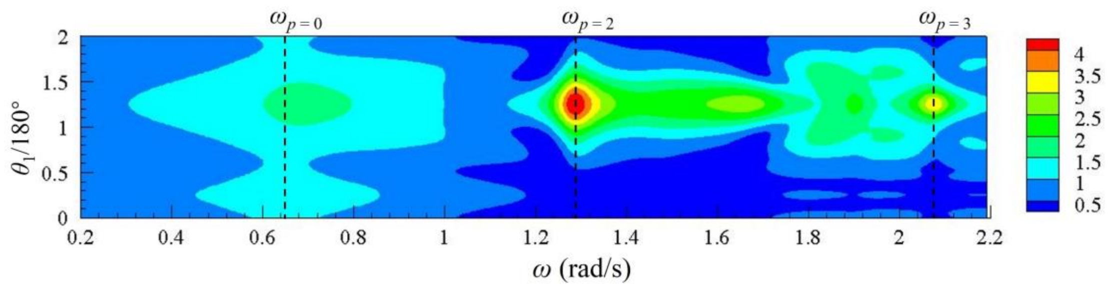

Fig. 9 Variation of the first-order wave run-up amplitude along the downstream column in an array of four circular columns with β = 45°.

As shown in Fig. 9, the peak wave run-up along the downstream cylinder appears at the up-wave point (θ_1 = 225°). Hereinafter, this point is named the featured point G_1. The location of G_1 is also given in Fig. 1. The first-order incident potential can be expressed in a Fourier series in terms of the polar angle θ:

$$\phi_I^{(1)}(r, \theta, z, \omega) = \sum_{m=0}^{+\infty}\left[\varphi_{I,m}^{(1)}(r, z, \omega)\cdot\cos m\theta\right], \tag{19}$$

where

$$\varphi_{I,m}^{(1)}(r, z, \omega) = -\frac{\mathrm{i}Ag}{\omega}\frac{\cosh\left[k(z+h)\right]}{\cosh(kh)}\varepsilon_m \mathrm{i}^m e^{-\mathrm{i}m\beta}J_m(kr). \tag{20}$$

In Eq. (20), ε_0 = 1, and ε_m = 2 when $m \geq 1$; $J_m(\cdot)$ is the Bessel function of order m. Correspondingly, the first-order wave run-up is decomposed into the following form:

$$\eta^{(1)}(x, y, \omega) = \sum_{m=0}^{+\infty}\left[\eta_m^{(1)}(x, y, \omega)\cdot\cos m\theta\right], \tag{21}$$

where $\eta_m^{(1)}$ represents the wave run-up component caused by the mth order Fourier component of incident waves. Fig. 10 depicts the variation of the first-order wave run-up amplitude at the featured point G_1. It illustrates that the amplification of the wave run-up owing to near trapping is more apparent at β = 45° compared to other wave headings, i.e., β = 0°, 15° and 30°. Fig. 11 shows the variation of the wave run-up components at G_1. It demonstrates that the noticeable peak wave run-up at ω = 0.652, 1.280 and 2.078 rad/s are mainly contributed by the 0th, 2nd and 3rd order Fourier component. In view of this, the near-trapped modes at these three frequencies are named p = 0, 2 and 3 modes, respectively. In addition, $\omega_{p=0}$, $\omega_{p=2}$ and $\omega_{p=3}$ are used to denote the near-trapping frequencies for p = 0, 2 and 3 modes, respectively. Among the three near-trapped modes, the complex wavenumber corresponding to the p = 2 mode has the smallest imaginary wavenumber component. It indicates that the p = 2 mode is the closest to pure-trapping with rather weak damping due to wave radiation to infinity, and therefore has the largest response when excited by incoming waves.

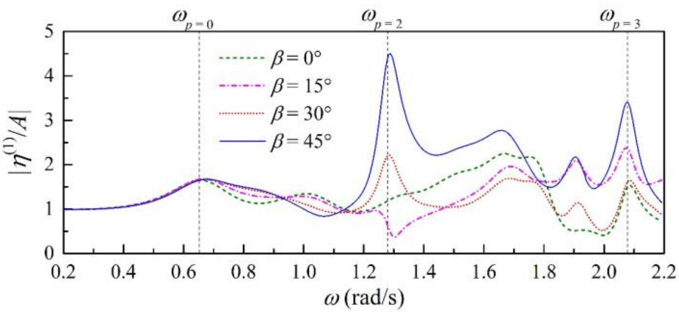

Fig. 10 Variation of the linear wave run-up amplitude at the featured point G_1 for an array of four circular columns.

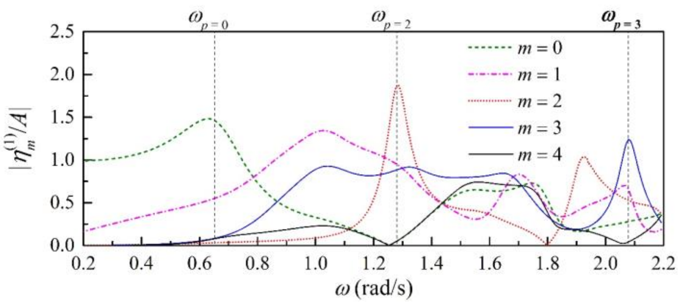

Fig. 11 Variation of the linear wave run-up components at the featured point G_1 for an array of four circular columns with β = 45°.

The mode shapes for different near-trapped modes are shown in Fig. 12. The near-trapped modes can be regarded as a mixture of both standing waves and outward propagating radiation waves. Therefore, the mode shapes in Fig. 12 are different from those in Figs. 6~8 for pure wave trapping. They lose the characters of symmetry or anti-symmetry with respect to the *x*- or *y*-axis, and the peak wave run-up responses around different columns are no longer uniform.

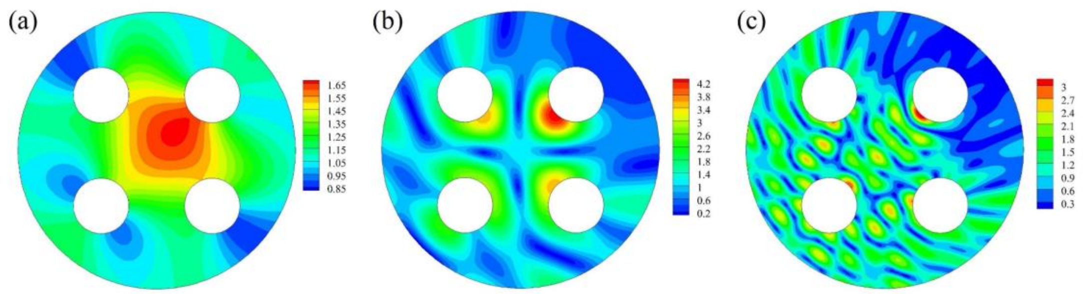

Fig. 12 Mode shapes for different near-trapped modes of an array of four circular columns with $\beta = 45°$: (a) $p = 0$, (b) $p = 2$, and (c) $p = 3$.

We then concern an array of rounded-corner square columns, a common type used to construct offshore structures. The configuration of the column array is the same as that in Fig. 1(b). Fig. 13 shows the variation of the linear wave run-up amplitude along the downstream column for $R = 6$ m and 8 m, respectively, with $\beta = 45°$. Meanwhile, the wave run-up amplitude at G_1 is plotted in Fig. 14 for different wave headings. As shown in Figs. 13 and 14, prominent local peaks are attained at 0.657, 1.315 and 2.155 rad/s, respectively, for $R = 6$ m. While for $R = 8$ m, the peak frequencies shift to 0.667, 1.304 and 2.122 rad/s, respectively. Those peak frequencies are close to the near-trapping frequencies of an array of circular columns but do not coincide exactly. It suggests that the near trapping could also occur in an array of rounded-corner square columns, and give rise to the noticeable amplification of wave run-up. In addition, the change in the corner ratio R/a leads to a slight shift in the near-trapping frequencies. For the $p = 0$ mode, in which the entrapped fluid behaves like a 'piston', a decrease of the corner ratio could reduce the inertia of the entrapped fluid, which in turn shifts the near-trapping frequency to the low-frequency region. While for the $p = 2$ and 3 modes, the fluid oscillates along the diagonal line of the column array. As the corner ratio decreases, the distance between the columns on the diagonal line is reduced, shifting the near-trapping frequency to the high-frequency region.

A comparison of the mode shapes between different corner ratios, i.e., $R/a = 0.6$, 0.8 and 1.0, is shown in Fig. 15. A corner ratio of $R/a = 1.0$ represents a limiting case of a circular column. The mode shapes corresponding to different corner ratios follow a similar trend. The amplification of the wave run-up is most pronounced at G_1. In addition, the change in the corner ratio can impose an evident impact on the wave run-up response at G_1. Since the rounded-corner square columns have flat panel parts, there is stronger wave reflection between adjacent columns than circular ones. With a lower corner ratio, circular cylinders evolves into square cylinders. The resultant parallel side faces from lines of square cylinders would lead to stronger reflection of waves. It is noted that such strong reflection would superimpose the local wave field and enhance the maximum wave run-up for $p = 0$ and $p = 2$ modes. While a reversed trend is observed from the $p = 3$ mode, in which the maximum response generally decreases with the decreasing corner ratio.

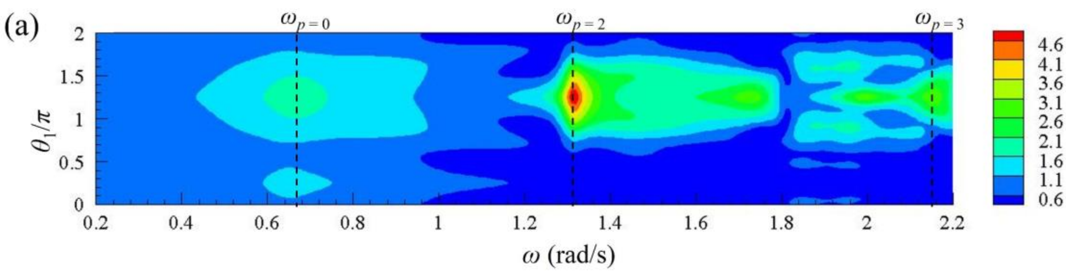

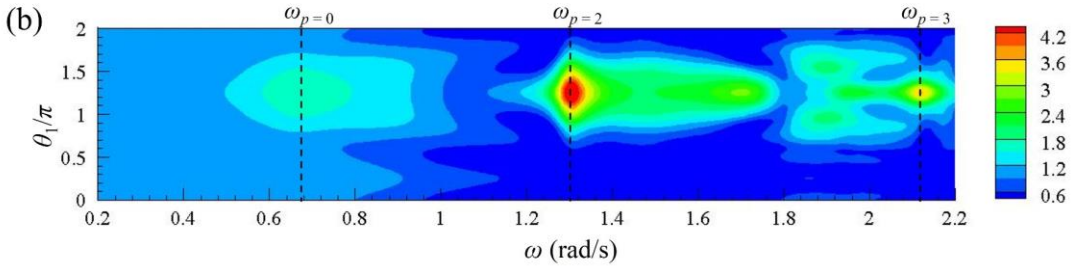

Fig. 13 Variation of the linear wave run-up amplitude along the downstream column in an array of four rounded-corner square columns with β = 45°: (a) R = 6 m, and (b) R = 8 m.

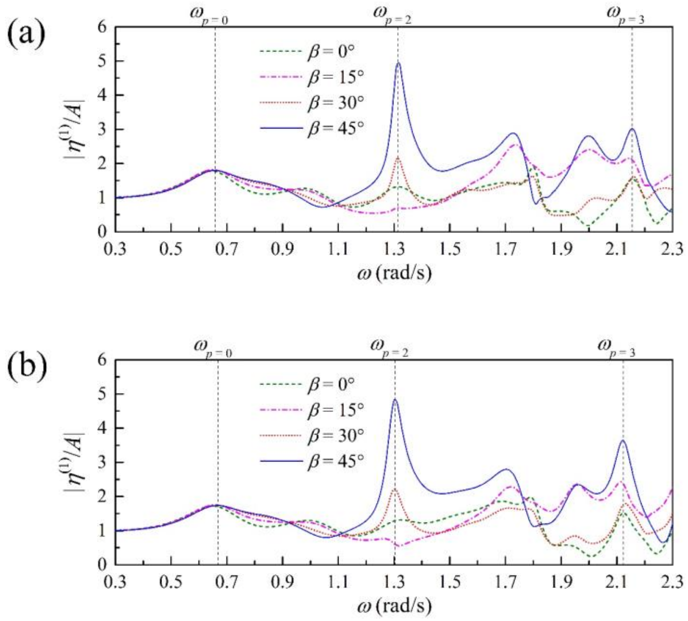

Fig. 14 Variation of the linear wave run-up amplitude at the featured point G_1 for an array of four rounded-corner square columns: (a) R = 6 m, and (b) R = 8 m.

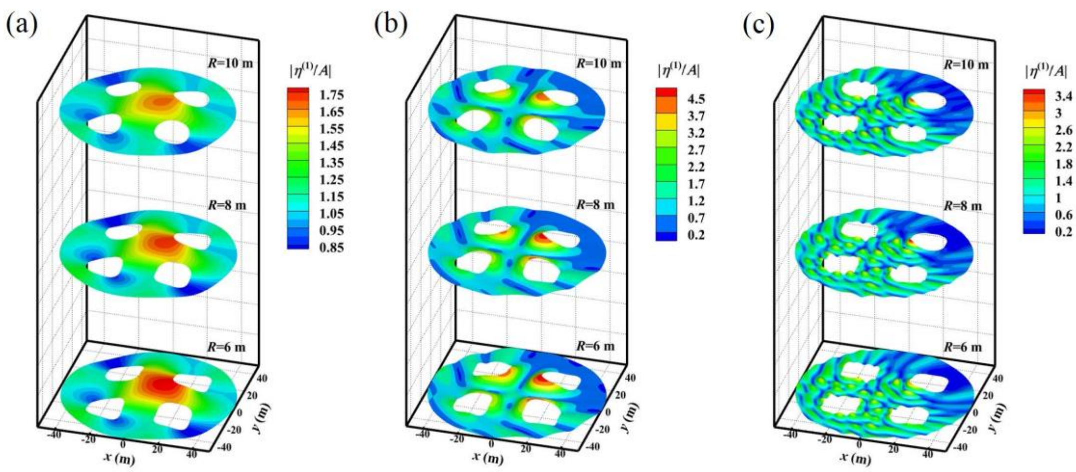

Fig. 15 Comparison of the mode shapes for an array of four rounded-corner square columns with β = 45°: (a) p = 0, (b) p = 2, and (c) p = 3.

5.2 Second-order near trapping and near-trapped modes in bi-chromatic seas

In order to avoid possible near trappings, traditionally, offshore structures have been designed so that the near-trapping frequency does not fall into the frequency range of significant ocean waves. However, in an irregular sea state, consisting of a superposition of regular wave components, two or more wave components that act together can generate higher-order waves at the sum- or difference-frequencies of a pair of combining components. The sum- and difference-frequency excitations cover a wide frequency range and may be of primary concern when they are close to the near-trapping frequencies of structures. The second-order near trapping is then concerned in this section. For the results presented in this section, the second-order sum- and difference-frequency free-surface elevations are divided by $A_j A_l$ and $A_j A_l^*$, respectively, customarily defined as the quadratic transfer functions (QTFs).

The configuration of a square array of circular columns (see Fig. 1(a)) is the first concern. Besides G_1, another three featured points, namely G_2, G_3 and G_4 are adopted. G_4 is at the centre of the internal free surface. In addition, G_2 and G_3 are located on the surface of the columns in Quadrant 2 and Quadrant 3, respectively. Fig. 16 plots the second-order sum-frequency free-surface elevation QTFs at the featured points G_1, G_2, G_3 and G_4 for different frequency combinations with $\beta = 45°$. Fig. 16 is characterised by the remarkable amplification of the free-surface elevation when $\omega_j + \omega_l = \omega_{p=2}$, which is most visible at G_1 among different featured points. It indicates that the near trapping could also occur in second order when the frequency of sum-frequency waves is close to the near-trapping frequency. As the second-order free-surface elevation holds a symmetric relation (see Eq. (13)), the results in Fig. 16 are symmetric with respect to the leading diagonal.

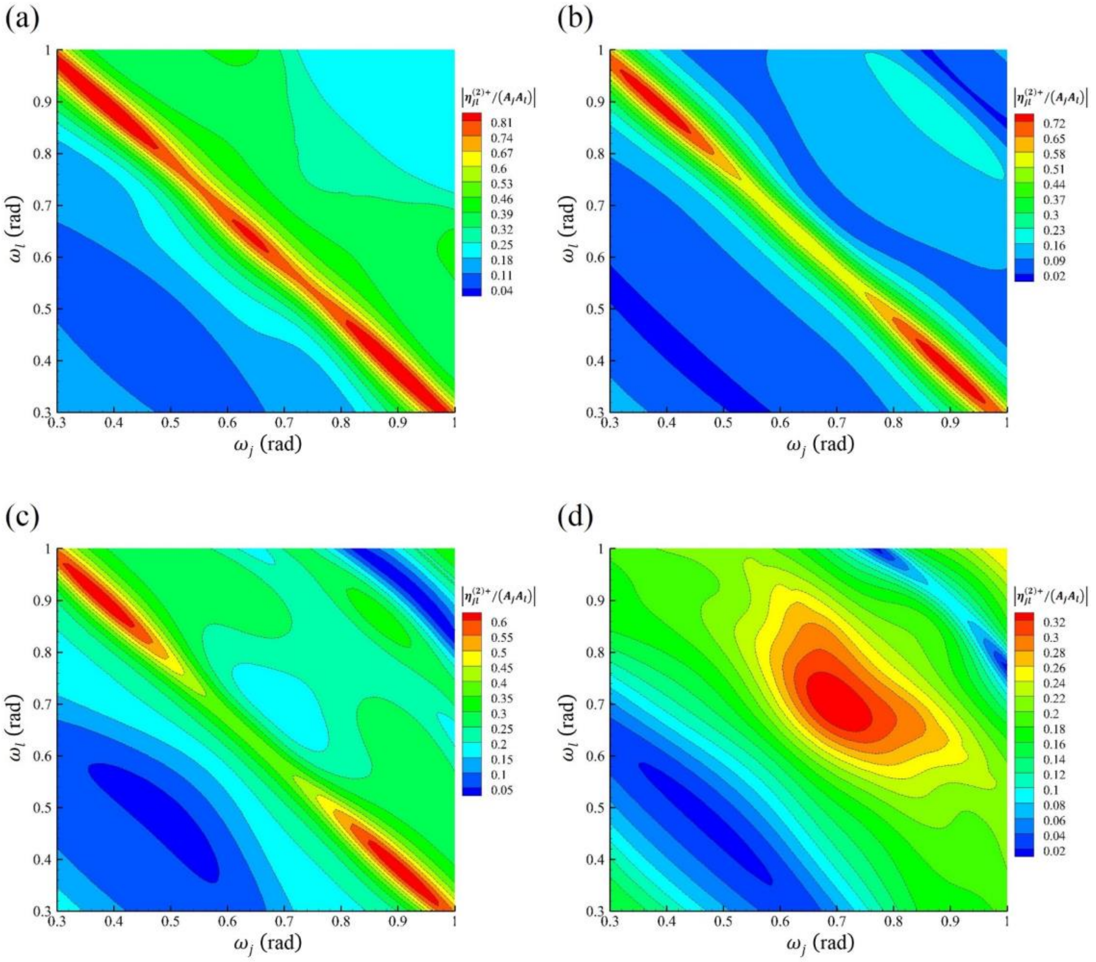

Fig. 16 Sum-frequency free-surface elevation QTFs $\left|\eta_{jl}^{(2)+}/\left(A_jA_l\right)\right|$ at the featured points G_1, G_2, G_3 and G_4 for a square array of circular columns with $\beta = 45°$: (a) G_1, (b) G_2, (c) G_3, and (d) G_4.

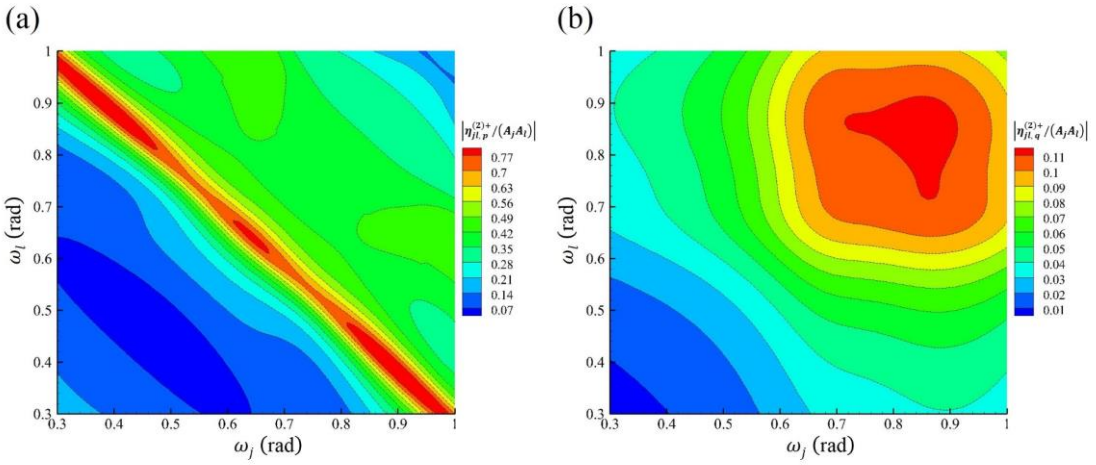

Fig. 17 'Potential-wave' and 'quadratic-wave' components of the sum-frequency free-surface elevation at the featured points G_1 for a square array of circular columns with $\beta = 45°$: (a) $\left|\eta_{jl,\,p}^{(2)+}/\left(A_jA_l\right)\right|$, and (b) $\left|\eta_{jl,\,q}^{(2)+}/\left(A_jA_l\right)\right|$.

As shown in Eq. (10), the sum-frequency free-surface elevation can be split into the 'potential wave' $\eta_{jl,p}^{(2)+}$ and the 'quadratic wave' component $\eta_{jl,q}^{(2)+}$. The variation of the two distinct components with respect to the frequency combination is plotted in Fig. 17. Fig. 17 shows clearly a ridge of high amplitude running perpendicular to the leading diagonal at a response frequency around $\omega_j + \omega_l = \omega_{p=2}$. It is noted that around $\omega_j + \omega_l = \omega_{p=2}$, $\eta_{jl,p}^{(2)+}$ is predominated, and follows a similar trend to that of $\eta_{jl}^{(2)+}$. It suggests that $\eta_{jl,p}^{(2)+}$ takes the primary responsibility for the second-order near trapping.

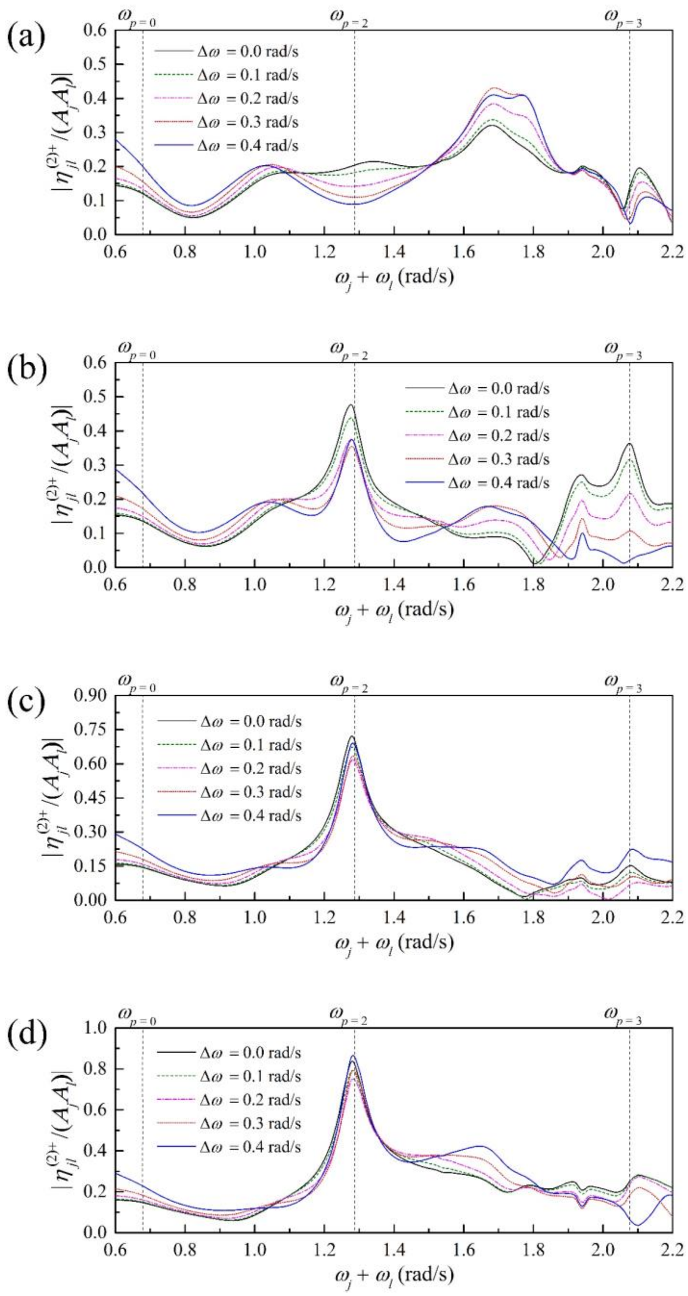

Fig. 18 Variation of the second-order sum-frequency wave run-up amplitude at the featured point G_1 for an array of circular columns for different frequency differences: (a) β = 0°, (b) β = 15°, (c) β = 30°, and (d) β = 45°.

The sum-frequency wave run-up amplitudes at G_1 for different frequency differences, i.e., $\Delta\omega$ = $\omega_j - \omega_l$ = 0.0, 0.1, 0.2, 0.3 and 0.4 rad/s, are shown in Fig. 18 for β = 0°, 15°, 30° and 45°, respectively. Noticeable application of wave run-up appears around $\omega_j + \omega_l = \omega_{p=2}$, which is most pronounced when β = 45°. This is consistent with the observation from the linear near trapping. Compared to the p = 2 mode, the near trapping at p = 0 and 3 modes have much less impact on the sum-frequency wave run-up. This can be explained from two aspects. One is that for p = 0 and 3 modes, the imaginary part of the complex wavenumbers is much larger, causing a larger amount of waves radiated to the far-field region and a weaker free-surface oscillation in the near-field region. The other can be attributed to that when $\omega_j + \omega_l$ is close to $\omega_{p=0}$ or $\omega_{p=3}$, $\eta_{jl,q}^{(2)+}$ is comparable to $\eta_{jl,p}^{(2)+}$ which is mainly responsible for the second-order near trapping. Then, $\eta_{jl,q}^{(2)+}$ can make a noticeable disturbance to the wave field and suppress the rising wave run-up caused by $\eta_{jl,p}^{(2)+}$.

Fig. 19 depicts the mode shapes for the p = 2 near-trapped mode in second order with the frequency difference varying as $\Delta\omega$ = 0.0, 0.2 and 0.4 rad/s. It is noted that both the linear and second-order near-trapped modes follow a similar trend. They own the common characteristics of generating the dominated peak at the up-wave point of the downstream column and forming nearly standing wave motions between neighbouring columns. It is also noted that the frequency difference imposes a negligible impact on the mode shape in the second order. This can be explained by the fact that the p = 2 mode is a lower-order near-trapped mode, and the corresponding near-trapping frequency is not high. The p = 2 mode can be excited at second order by the frequency combination of $\left(\omega_{p=2}/2 \mp \Delta\omega/2,\ \omega_{p=2}/2 \pm \Delta\omega/2\right)$. The corresponding linear incident waves are in the low-frequency region and have long wavelengths, resulting in weak scattering in the linear wave fields. As a result, when $\omega_j + \omega_l = \omega_{p=2}$, the adjustment of $\Delta\omega$ does not apparently affect the second-order near-trapping response which depends much on the linear wave fields.

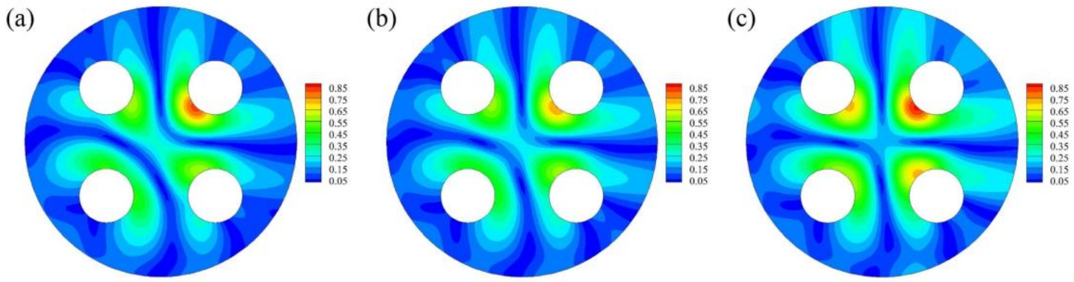

Fig. 19 Mode shapes for the p = 2 near-trapped mode at second order of a square array of circular columns with β = 45° for different frequency differences: (a) $\Delta\omega$ = 0.0 rad/s, (b) $\Delta\omega$ = 0.2 rad/s, and (c) $\Delta\omega$ = 0.4 rad/s.

An array of rounded-corner square columns is then considered. The sum-frequency wave run-up amplitudes at G_1 are presented in Figs. 20~21 for different frequency differences and wave headings. Figs. 20~21 clearly exhibit the occurrence of near trapping at $\omega_j + \omega_l = \omega_{p=2}$. As shown in Fig. 22, the mode shapes corresponding to different corner ratios follow a similar trend. When β = 45°, the pronounced wave run-up at the featured point G_1 gets gradually enhanced with decreasing corner ratio, which is consistent with the observation from the linear near trapping. This can be attributed to the stronger wave reflection between columns with a lower corner ratio.

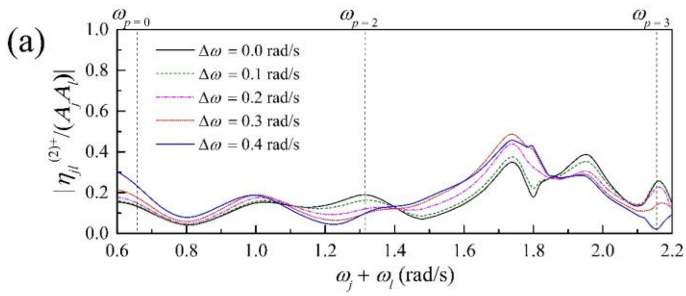

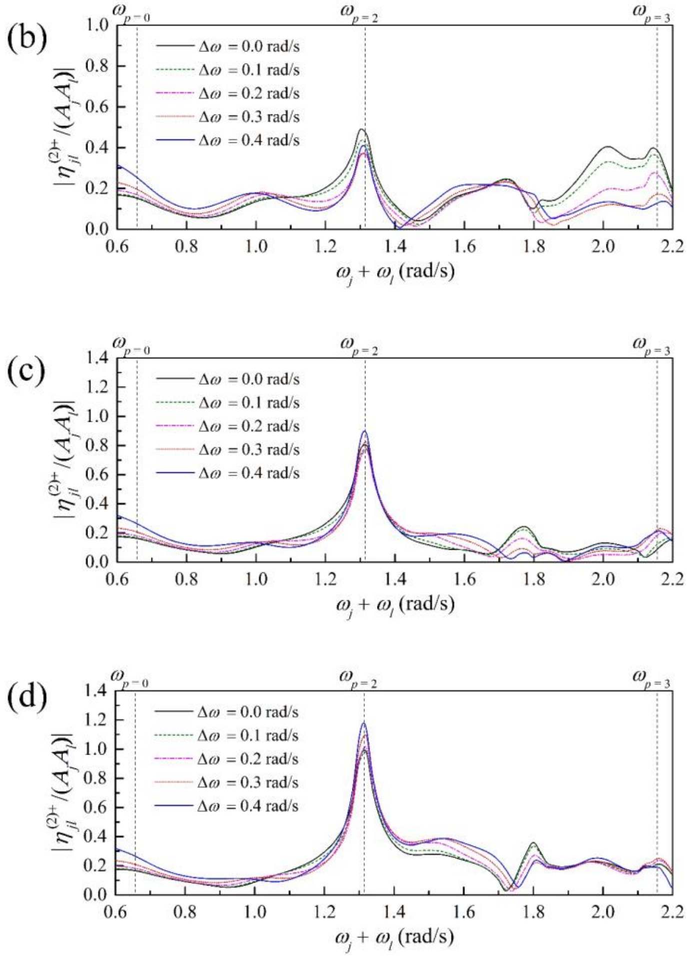

Fig. 20 Variation of the second-order sum-frequency wave run-up amplitude at the featured point G_1 for an array of rounded-corner square columns with R = 6 m for different frequency differences: (a) β = 0°, (b) β = 15°, (c) β = 30°, and (d) β = 45°.

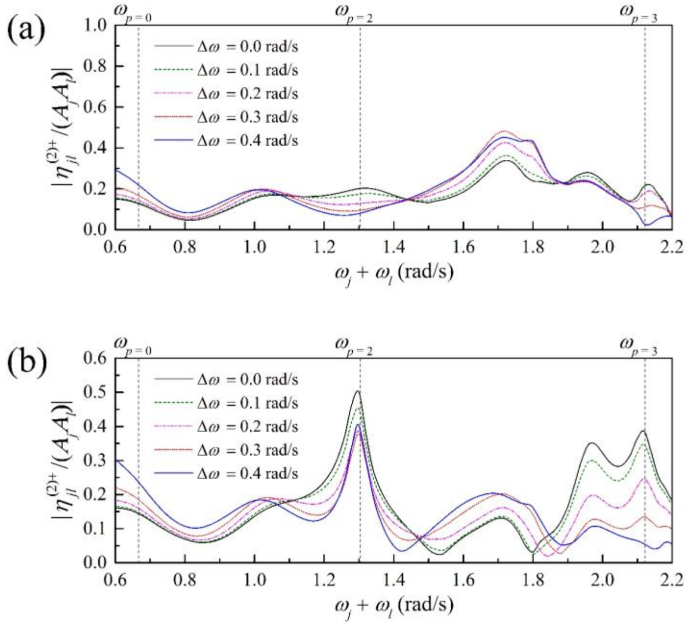

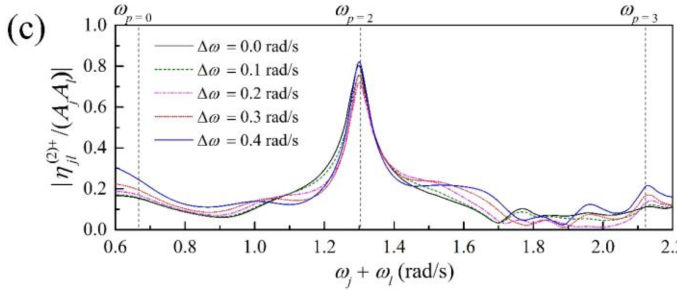

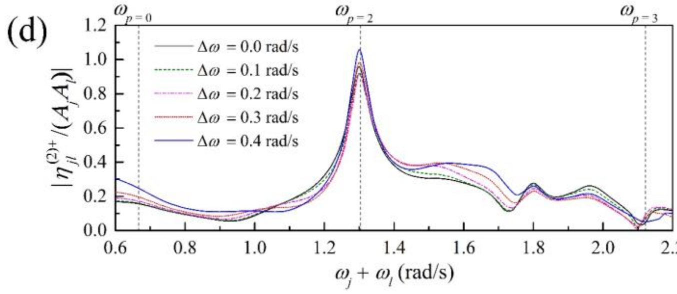

Fig. 21 Variation of the second-order sum-frequency wave run-up amplitude at the featured point G_1 for an array of rounded-corner square columns with R = 8 m for different frequency differences: (a) β = 0°, (b) β = 15°, (c) β = 30°, and (d) β = 45°.

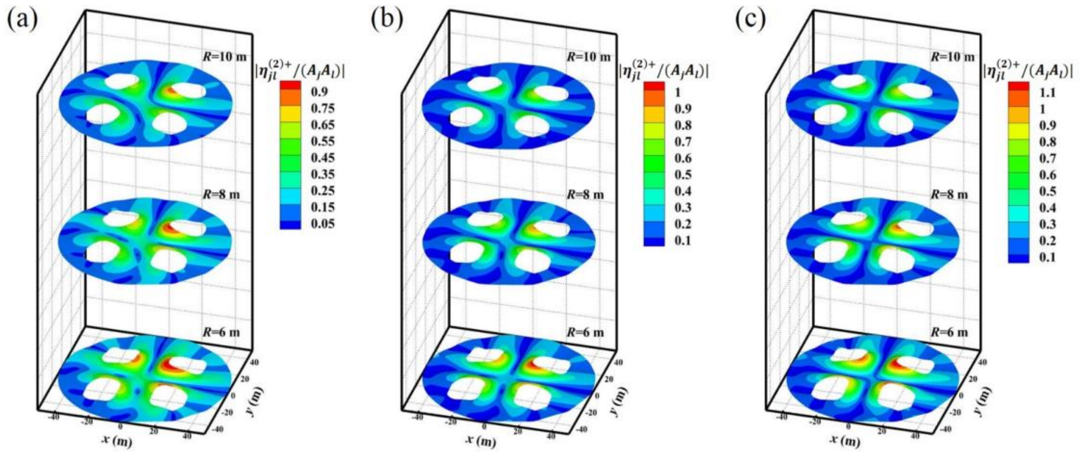

Fig. 22 Comparison of the mode shapes for the p = 2 near-trapped mode at second order of an array of rounded-corner square columns with β = 45°: (a) $\Delta\omega$ = 0.0 rad/s, (b) $\Delta\omega$ = 0.2 rad/s, and (c) $\Delta\omega$ = 0.4 rad/s.

The second-order difference-frequency wave run-up amplitude and its constituent components at the featured point G_1 are shown in Fig. 23 for an array of circular columns with β = 45°. Narrow-banded seas are assumed, and the frequency difference $\Delta\omega$ varies from 0.0 rad/s to 0.4 rad/s. Analogous results to those in Fig. 23 but for rounded-corner square columns are shown in Fig. 24~25. As the excitation frequency is away from the near-trapping frequency, the second-order near trapping cannot be excited by the difference-frequency waves, and a significant amplification of $\eta_{jl,\,p}^{(2)-}$ cannot be formed. When ω_j or ω_l is close to $\omega_{p=2}$, the amplified first-order wave fields can give rise to the notable enhancement of $\eta_{jl,\,q}^{(2)-}$ and $\eta_{jl,\,p}^{(2)-}$. The amplification of $\eta_{jl,\,q}^{(2)-}$ is much more obvious than that of $\eta_{jl,\,p}^{(2)-}$, and leads to the noticeable amplification of $\eta_{jl}^{(2)-}$.

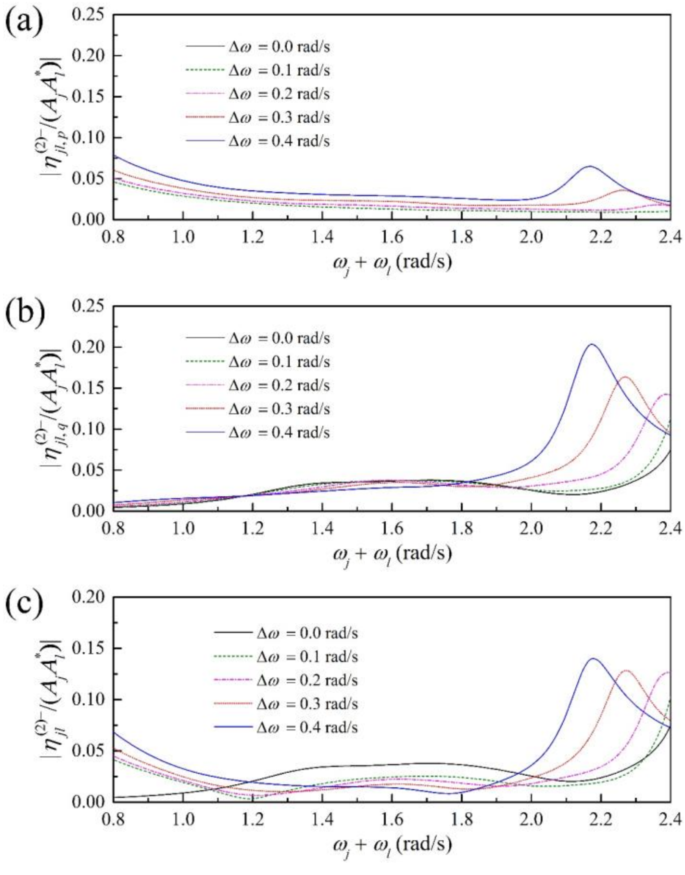

Fig. 23 Variation of the second-order difference-frequency wave run-up amplitude and its constituent components at the featured point G_1 for an array of circular columns with $\beta = 45°$: (a) $\eta_{jl,\,p}^{(2)-}$, (b) $\eta_{jl,\,q}^{(2)-}$, and (c) $\eta_{jl}^{(2)-}$.

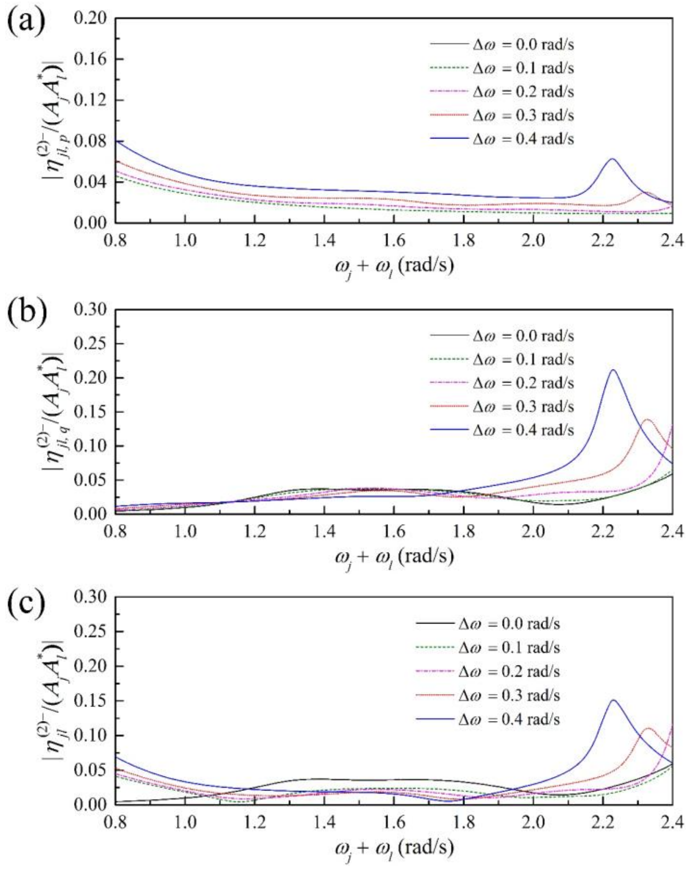

Fig. 24 Variation of the second-order difference-frequency wave run-up amplitude and its constituent components at the featured point G_1 for an array of rounded-corner square columns (R = 6 m) with $\beta = 45°$: (a) $\eta^{(2)-}_{jl,p}$, (b) $\eta^{(2)-}_{jl,q}$, and (c) $\eta^{(2)-}_{jl}$.

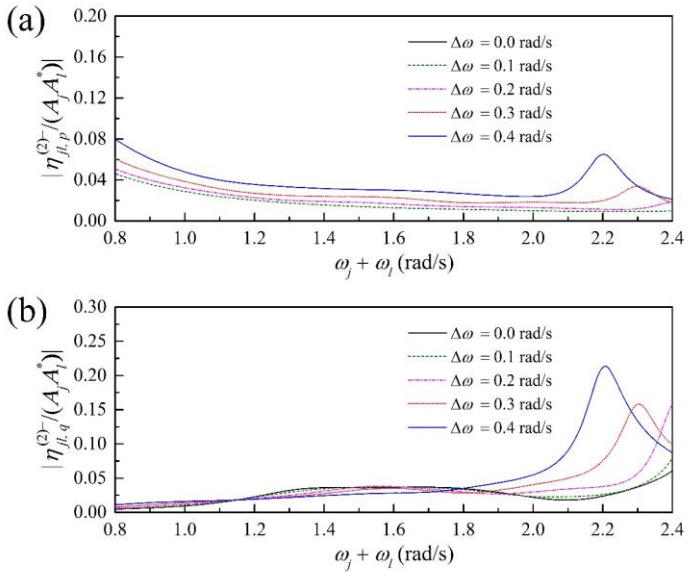

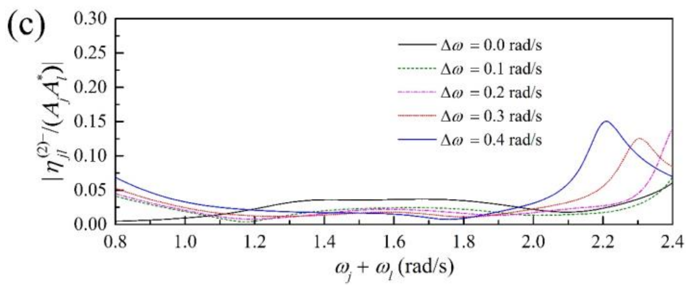

Fig. 25 Variation of the second-order difference-frequency wave run-up amplitude and its constituent components at the featured point G_1 for an array of rounded-corner square columns (R = 8 m) with β = 45°: (a) $\eta_{jl,p}^{(2)-}$, (b) $\eta_{jl,q}^{(2)-}$, and (c) $\eta_{jl}^{(2)-}$.

5.3 Approximation of the free-surface elevation QTFs for the second-order near trapping

The QTF for the second-order free-surface elevation contains the 'potential wave' component as well as the 'quadratic wave' component. The latter can be easily obtained from the linear wave fields. While the former is much more computationally intensive and requires a complete solution of the second-order boundary-value problem. For an irregular wave train that can be regarded as the superposition of N harmonic wave components, an N×N matrix of QTFs is usually required. Therefore, it is beneficial to find a method that can facilitate the calculation of the complicated 'potential wave' component and in turn reduce the computational burden of QTFs

Fig. 17(a) shows that for a square array of columns, $\eta_{jl,p}^{(2)+}$ is approximately constant close to but perpendicular to the leading diagonal. This has been explained by Taylor et al. (2007) and Grice et al. (2015), in which the incident waves at low frequencies were primarily concerned. $\eta_{jl,p}^{(2)+}$ is a function of the frequency pair (ω_j, ω_l). $\omega_j+\omega_l$ is the response frequency of the sum-frequency free-surface elevation, and $\Delta\omega$ is the distance away from the leading diagonal in a plot of $\eta_{jl,p}^{(2)+}$ versus (ω_j, ω_l). $\eta_{jl,p}^{(2)+}$ can be further separated into two parts: the 'free waves' and the 'phase-locked waves', respectively (Molin, 1979). The former part is resulted from the scattering of incoming waves and satisfies a homogeneous boundary condition on the free surface. In contrast, the later part is driven by the free-surface forcing terms and locked to the first-order wave system. The effect of the wave scattering process largely depends on the wave-length. For the part of free waves, its wavelength and the frequency sum $\omega_j + \omega_l$ satisfies the dispersion equation. Therefore, the frequency difference $\Delta\omega$ is not likely to impose a remarkable effect on the scattered wave field for each frequency pair with the same frequency sum. This is especially true at low frequencies where the dimensions of the column array are fairly small relative to the wavelengths of linear incident waves. At low frequencies, the wave diffraction by the linear incident waves is not evident, and linear incident wave fields are not significantly disturbed. As a result, at low frequencies, there can be a minor variation of the free-surface forcing term with respect to $\Delta\omega$, and the phase-locked waves cannot vary significantly with the distance from the leading diagonal.

An approximate method is then developed to evaluate the free-surface elevation QTFs. In this method, the 'quadratic wave' component $\eta_{jl,q}^{(2)+}$ is evaluated exactly; while the 'potential wave' component $\eta_{jl,p}^{(2)+}$ is assumed to be dependent on the response frequency $\omega_j + \omega_l$ far more than the frequency difference $\Delta\omega$. Then, in a plot of $\eta_{jl,p}^{(2)+}$ versus (ω_j, ω_l), $\eta_{jl,p}^{(2)+}$ is assumed to be constant perpendicular to the leading diagonal, and the off-diagonal term is approximated by the diagonal one. Then, $\eta_{jl}^{(2)+}$ is approximately evaluated based on the following expression:

$$\eta_{jl}^{(2)+}\left(\omega_j,\ \omega_l\right) = \eta_{jl,q}^{(2)+}\left(\omega_j,\ \omega_l\right) + \eta_{jl,p}^{(2)+}\left(\hat{\omega},\ \hat{\omega}\right) + O\left(\Delta\omega\right), \tag{22}$$

where $\hat{\omega} = \left(\omega_j + \omega_l\right)/2$. In the computation, only the first two terms on the right-hand side of Eq. (22) are evaluated, the leading order of the ignored part being $\Delta\omega$. For an irregular wave train composed of N harmonic wave components, this method allows the number of the lengthy calculation of the 'potential wave' component to be reduced to just N.

A comparison between the results based on the approximate method and the complete solution is made to assess the usefulness of the proposed approximation (see Figs. 26~27). Results are in good agreement when close to the leading diagonal, such as $\Delta\omega$ = 0.1 rad/s. In addition, for a higher $\Delta\omega$, satisfactory agreement can be observed in the low-frequency region. The approximate approach is based on the hypothesis of weakly scattering of the linear wave fields, which is especially true for long incident waves. As the wave frequencies of the dual incident waves increase, the wavelengths gradually get shorter, and wave scattering process gets stronger, making the weakly scattering hypothesis less reliable. In addition, for a fixed frequency sum $\omega_j + \omega_l$, as the frequency difference $\Delta\omega = \omega_j - \omega_l$ increases, one wave component of the dual incident waves moves gradually into the high-frequency region. This can enhance the wave scattering process, and then affect the effectiveness of the approximate approach. As a result, this approximation becomes less reliable when further away from the diagonal and at higher frequencies

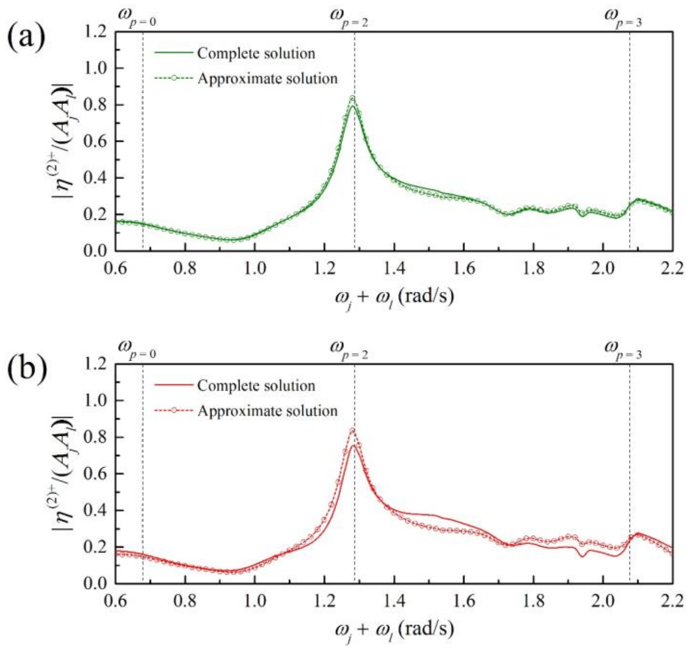

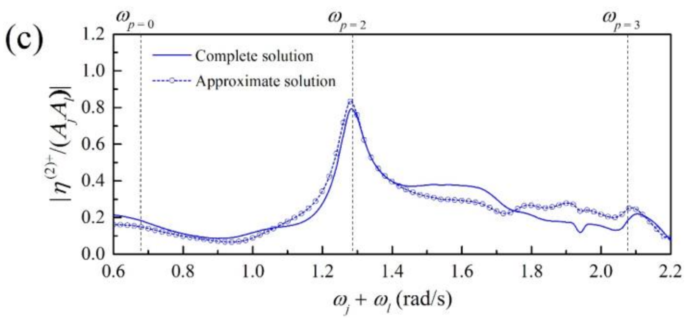

Fig. 26 A comparison between the second-order sum-frequency free-surface elevation based on the approximate method and the complete solution at the featured point G_1 for an array of circular columns with β = 45°: (a) $\Delta\omega$ = 0.1 rad/s, (b) $\Delta\omega$ = 0.2 rad/s, and (c) $\Delta\omega$ = 0.3 rad/s.

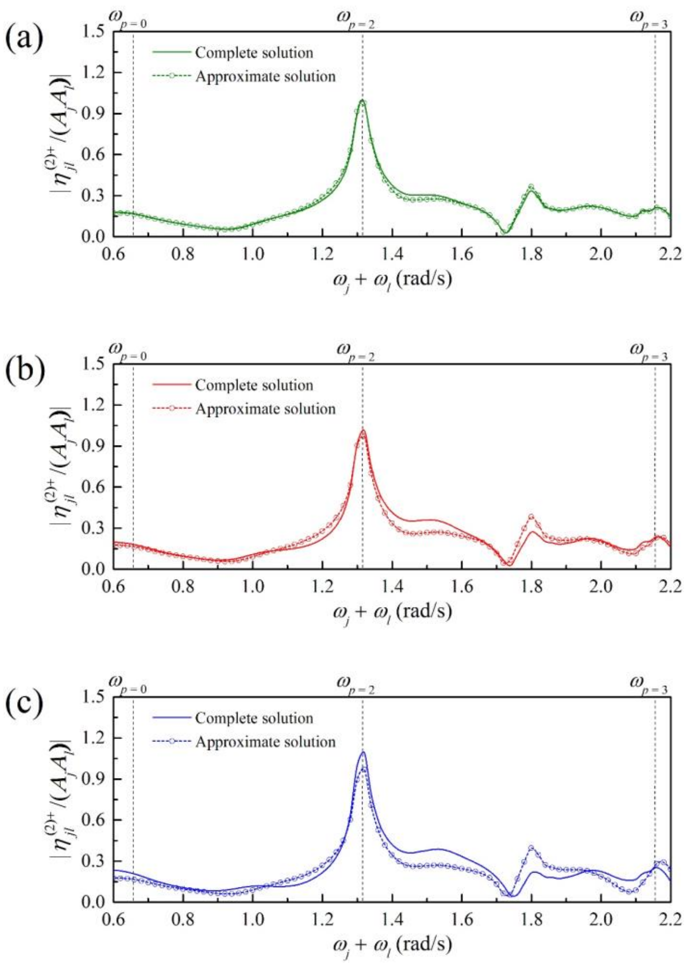

Fig. 27 A comparison between the second-order sum-frequency free-surface elevation based on the approximate method and the complete solution at the featured point G_1 for an array of rounded-corner square (R = 6 m) columns with β = 45°: (a) $\Delta\omega$ = 0.1 rad/s, (b) $\Delta\omega$ = 0.2 rad/s, and (c) $\Delta\omega$ = 0.3 rad/s.

6. Conclusions

A numerical investigation has been conducted for the near trapping of water waves by a square array of vertical columns. The bi-chromatic waves have been used to drive the response in the second order. Near-trapping responses have been excited successfully through the complicated wave–structure interactions, i.e., the linear excitation or nonlinear process. The main conclusions of this research are summarised as follows:

1) Numerical results indicate that a four-column cluster can bring about the prominent near-trapping phenomenon, accompanied by the noticeably amplified free-surface oscillation around the columns. Three lower-order near-trapped modes, namely $p = 0$, 2 and 3 modes, are primarily concerned, among which the $p = 2$ mode has the smallest imaginary part of the complex wavenumber and most pronounced response. For a specific pair of incident waves, when the frequency sum is consistent with the near-trapping frequency, second-order near trapping can then be induced. The second-order near-trapping response is dominated by the 'potential wave' component, while the 'quadratic wave' component plays a secondary role.

2) The $p = 2$ near-trapped mode caused by the linear and second-order excitations own the common characteristics. For a diamond arrangement, the dominated wave run-up is attained at the up-wave point of the down-stream column, and nearly standing wave motions are formed between neighbouring columns. In addition, when the frequency sum coincides with the near-trapping frequency, the frequency difference is found to impose negligible impact on the mode shape in the second order, which is at least true when $\Delta\omega$ is less than 0.4 rad/s. This can be attributed to the fact that the corresponding linear incident waves have long wavelengths for a lower-order near-trapped mode at second order, resulting in weak scattering in the linear wave fields. As a result, when the frequency sum is close to the near-trapping frequency of a lower-

order mode, the adjustment of the frequency combination does not apparently affect the second-order near-trapping response, which depends much on the linear wave fields.

3) Compared with the circular ones, the rounded-corner square columns have flat panel parts, giving rise to stronger wave reflection between the adjacent columns. A lower corner ratio corresponds to a larger parallel part of columns, which could enhance the hydrodynamic interference effect among the columns and promote the near-trapping response for the $p = 2$ mode. A decrease in the corner can reduce the distance between the columns on the diagonal line, shifting the near-trapping frequency of the $p = 2$ mode to the high-frequency region.

4) For the sum-frequency problem, the wavelength corresponding to the 'free waves' is much shorter than that of linear waves. It suggests that the scattering of the linear incident waves is much weaker than that in the second order. This is especially true in the low-frequency region, where the lower-order near-trapped modes at second order can be induced. In view of this, an approximate approach is developed for the second-order near-trapping response based on the assumption of weakly scattering of the linear wave fields. In this approximate approach, the 'quadratic wave' component is evaluated exactly, while the complicated 'potential wave' component corresponding to a pair of incident waves with distinct frequencies is approximated by that in mono-chromatic seas with mean frequency. Numerical results indicate that such approximation gives a reasonable prediction, especially in the low-frequency region and for a slight frequency difference.

Acknowledgement

The work is supported by the National Natural Science Foundation of China (Grant No. 51809037).

Reference

1. Archer A, Wolgamot H, Orszaghova J, Bennetts L G, Peter M A, Craster R V. Experimental observation of Rainbow Trapping of water waves. In Proceedings of the 35th International Workshop on Water Waves and Floating Bodies, Korea (Virtual), 2020.
2. Bai W, Feng X, Eatock Taylor R, Ang K K. Fully nonlinear analysis of near-trapping phenomenon around an array of cylinders. Applied Ocean Research, 2014, 44: 71-81.
3. Contento G, D'este F, Sicchiero M, Codiglia R, Calzà M. Run-up and wave forces on an array of vertical circular cylinders: Experimental study on second-order near trapping. International Journal of Offshore and Polar Engineering, 2005, 15: 402-409.
4. Cong P W, Gou Y, Teng B. Effect of pontoons on free surface elevation around a TLP platform. Science China Technological Sciences, 2014, 57(1): 163-180.
5. Cong P W, Gou Y, Teng B, Zhang K, Huang Y. Model experiments on wave elevation around a four-cylinder structure. Ocean Engineering, 2015, 96: 40-55.
6. Cong P W, Chen L F, Gou Y. Hydrodynamic interaction among multiple columns in front of a vertical wall. Ocean Engineering, 2020, 197: 106877.
7. Cong P W, Teng B, Bai W. Second-order wave run-up on a vertical cylinder adjacent to a plane wall based on the application of quadratic transfer function in bi-directional waves. Marine Structures, 2021, 76: 102879.
8. Eatock Taylor R, Chau F P. Wave diffraction theory—Some developments in linear and nonlinear theory. 1992, 114(3): 185-194.
9. Evans D V, Porter R. Near-trapping of waves by circular arrays of vertical cylinders. Applied Ocean Research, 1997, 19(2): 83-99.
10. Grice J R, Taylor P H, Eatock Taylor R. Near-trapping effects for multi-column structures in deterministic and random waves. Ocean engineering, 2013, 58: 60-77.
11. Grice J R, Taylor P H, Eatock Taylor R, Zang J, Walker D A G. Extreme wave elevations beneath offshore platforms, second order trapping, and the near flat form of the quadratic transfer functions. Computers & Fluids, 2015, 119: 13-25.
12. Göteman M, Engström J, Eriksson M, Isberg J. Optimizing wave energy parks with over 1000 interacting point-absorbers using an approximate analytical metho. International Journal of Marine Energy, 2015, 10: 113-126.
13. Göteman M. Wave energy parks with point-absorbers of different dimensions. Journal of Fluids and Structures, 2017, 74: 142-157.

14. Kagemoto H, Yue D K P. Interactions among multiple three-dimensional bodies in water waves: an exact algebraic method. Journal of Fluid Mechanics, 1986, 166: 189-209.
15. Kagemoto H, Murai M, Fujii T. Second-order resonance among an array of two rows of vertical circular cylinders. Applied Ocean Research, 2014, 47: 192-198.
16. Kashiwagi M, Iida T, Miki M. Wave drift force on floating bodies of cloaking configuration and associated wave patterns. In Proceedings of the 30th International Workshop on Water Waves and Floating Bodies, UK, Bristol, 2015.
17. Kim M H, Yue D K P. The complete second-order diffraction solution for an axisymmetric body Part 2. Bichromatic incident waves and body motions. Journal of Fluid Mechanics, 1990, 211: 557-593.
18. Linton C M, Evans D V. The interaction of waves with arrays of vertical circular cylinders. Journal of Fluid Mechanics, 1990, 215: 549-569.
19. Lu L, Zhou Z B, Qin J M, Song Z W, Xie Z H, Lou X F, Li Y C. Three-dimensional viscous numerical simulations of focused waves on bottom-mounted multiple rigid circular cylinders. International Journal of Offshore and Polar Engineering, 2021, 31(01): 61-70.
20. Maniar H D, Newman J N. Wave diffraction by a long array of cylinders. Journal of Fluid Mechanics, 1997, 339: 309-330.
21. Malenica S, Eatock Taylor R, Huang J B. Second-order water wave diffraction by an array of vertical cylinders. Journal of Fluid Mechanics, 1999, 390: 349-373.
22. Ma Q W, Wu G X, Eatock Taylor R. Finite element simulations of fully non−linear interaction between vertical cylinders and steep waves. Part 2: numerical results and validation. International Journal for Numerical Methods in Fluids, 2001, 36(3): 287-308.
23. Meylan M H, Eatock Taylor R. Time-dependent water-wave scattering by arrays of cylinders and the approximation of near trapping. Journal of Fluid Mechanics, 2009, 631: 103-125.
24. Molin B. Second-order diffraction loads upon three-dimensional bodies. Applied Ocean Research, 1979, 1(4): 197-202.
25. Newman J N. Cloaking a circular cylinder in deep water. In Proceedings of the 28th International Workshop on Water Waves and Floating Bodies, Marseille, France, 2013.
26. Newman J N. Cloaking a circular cylinder in water waves. European Journal of Mechanics-B/Fluids, 2014, 47: 145-150.
27. Ning D Z, Xu J, Chen L F, Cong P W, Zhao M, Jiang C B. Boussinesq modelling of near-trapping in a four-cylinder array. Ocean Engineering, 2022, 248: 110767.
28. Ohl C O G, Eatock Taylor R, Taylor P H, Borthwick A G L. Water wave diffraction by a cylinder

array. Part 1. Regular waves. Journal of Fluid Mechanics, 2001, 442: 1-32.
29. Ohl C O G, Taylor P H, Eatock Taylor R, Borthwick A G L. Water wave diffraction by a cylinder array. Part 2. Irregular waves. Journal of Fluid Mechanics, 2001, 442: 33-66.
30. Peter M A, Bennetts L G, Craster R V. Rainbow trapping of water waves. In Proceedings of the 33rd International Workshop on Water Waves and Floating Bodies, Guidel-Plages, France, 2018.
31. Peter M A, Bennetts L G, Craster R V. A graded resonator array for amplification of water waves. In Proceedings of the 34th International Workshop on Water Waves and Floating Bodies, Newcastle, Australia, 2019.
32. Ren X D, Tao L B, Liang Y B, Han D F. Nonlinear wave surface elevation around a multi-column offshore structure. Ocean Engineering, 2021, 238: 109757.
33. Sun L, Teng B, Ning D Z. A self-adaptive Gauss integral method for evaluation of nearly singular integrals. Journal of Dalian University of Technology, 2007, 1: 106-112. (In Chinese)
34. Taylor P H, Zang J, Walker D A G, Eatock Taylor R. Second order near-trapping for multi-column structures and near-flat QTFs. In Proceedings of the 22nd Internatioanl Workshop on Water Waves and Floating Bodies, Plitvice, Croatia. 2007: 15-18.
35. Teng B, Cong P W. A novel decomposition of the quadratic transfer function (QTF) for the time-domain simulation of non-linear wave forces on floating bodies. Applied Ocean Research, 2017, 65: 112-128.
36. Wang C Z, Wu G X. Time domain analysis of second-order wave diffraction by an array of vertical cylinders. Journal of Fluids and Structures, 2007, 23(4): 605-631.
37. Walker D A G, Eatock Taylor R, Taylor P H, Zang J. Wave diffraction and near-trapping by a multi-column gravity-based structure. Ocean Engineering, 2008, 35(2): 201-229.
38. Zhang Z G, He G H, Wang Z K, Liu S, Gou Y, Liu YY. Numerical and experimental studies on cloaked arrays of truncated cylinders under different wave directions. Ocean Engineering, 2019, 183: 305-317.
39. Zhang Z G, Liu S, Luan Z X, Wang Z K, He G H. Invisibility concentrator for water waves. Physics of Fluids, 2020a, 32(8): 081701.
40. Zhang Z G, He G H, Wang W, Liu S, Wang Z K. Broadband cloaking of multiple truncated cylinders in water waves using the arrangement defects. Physics of Fluids, 2020b, 32(6): 067111.
41. Zhang Z H, Tu J H, Wu L, He Y K, Ren H J, Zhang M M. Numerical investigation on the wave force characteristics of multi-cylinder with equilateral-triangular arrangement. Ocean Engineering, 2022, 243: 110245.